

1N-39

127095

P-35

Design of a High-Temperature Experiment for Evaluating Advanced Structural Materials

Theodore T. Mockler, Mario Castro-Cedeno,
and Herbert J. Gladden
Lewis Research Center
Cleveland, Ohio

and

Albert Kaufman
Analex Corporation
3001 Aerospace Parkway
Brook Park, Ohio

August 1992

(NASA-TM-105833) DESIGN OF A
HIGH-TEMPERATURE EXPERIMENT FOR
EVALUATING ADVANCED STRUCTURAL
MATERIALS (NASA) 35 p

N93-11624

Unclass

G3/39 0127095

NASA

**ORIGINAL CONTAINS
COLOR ILLUSTRATIONS**

DESIGN OF A HIGH-TEMPERATURE EXPERIMENT FOR EVALUATING ADVANCED STRUCTURAL MATERIALS

Theodore T. Mockler, Mario Castro-Cedeno,
and Herbert J. Gladden
National Aeronautics and Space Administration
Lewis Research Center
Cleveland, Ohio 44135

and

Albert Kaufman
Analex Corporation
Brook Park, Ohio 44142

Summary

This report describes the design of an experiment for evaluating monolithic and composite material specimens in a high-temperature environment and subject to high thermal gradients. The material specimens will be exposed to aerothermal loads that correspond to thermally similar engine operating conditions. Materials evaluated in this study were monolithic nickel alloys and silicon carbide. In addition, composites such as tungsten/copper were evaluated. A facility to provide the test environment has been assembled in the Engine Research Building at the Lewis Research Center. The test section of the facility will permit both regular and schlieren photography, thermal imaging, and laser Doppler anemometry. The test environment will be products of hydrogen-air combustion at temperatures from about 1200 °F to as high as 4000 °F. The test chamber pressure will vary up to 60 psia, and the free-stream flow velocity can reach Mach 0.9. The data collected will be used to validate thermal and stress analysis models of the specimen. This process of modeling, testing, and validation is expected to yield enhancements to existing analysis tools and techniques.

Introduction

The goal of doubling the capability of aircraft propulsion systems by the twenty-first century requires significant ad-

vances in material, structural, and aerothermodynamic technology (ref. 1). In particular, the engine hot-section components must function at peak efficiencies at 3000 °F to near stoichiometric temperatures and at high pressures with minimal cooling and without degradation of component life. The implications of these requirements can be contradictory. A lightweight, high-temperature material (such as metal-matrix composites or ceramic-matrix composites), either cooled or uncooled, must be fabricated in complex aerodynamic shapes for optimum aerothermal performance.

The development of complex structures made from high-temperature composite materials requires a comprehensive knowledge of the aerothermal loads imposed on the structures by the environment and the reaction of the structures to these loads. The objective of this research is to develop an understanding of the physics relating the aerothermal and mechanical loads and the material and structural responses of these components. A structure made of composite materials may be tailored to the expected aerothermal loads to take advantage of their strengths and minimize their weaknesses if these can be defined early in the design effort. The thermal and structural responses to these loads are also important because any structural deformations will also affect the character of the aerothermal loads.

A threefold approach to this task will be taken. A modular, user-friendly heat transfer and pressure loads definition code, which will generate a realistic range of loads, is being developed to provide input to a thermal analyzer, a structural analyzer, or both. In addition, an interdisciplinary baseline

calibration experiment to verify the code is being designed and constructed. Finally, an opportunity to evaluate composite materials, to test the ability of constitutive modeling codes, and to evaluate advanced sensors is provided through high-temperature experiments.

Work has begun on the aerothermal loads definition code and the interfaces necessary to allow interaction between the code and the thermal and structural analyzers. In addition, a high-temperature facility has been assembled that will be used to provide the data required to verify and calibrate the aerothermal loads code. This facility will also be used to evaluate various composite material specimens when they become available. It is critically important to know the boundary conditions on the test specimen in order to verify the aerothermal loads code and its interfaces with the thermal and structural analyzers. The capabilities of this facility will permit the detailed measurement of gas-stream temperature, pressure, and velocity. Surface phenomena, such as temperature and heat flux, can also be measured in some detail. When high-temperature strain gages are available, these measurements will also be made.

This report discusses the facility and the experimental hardware that will be used to evaluate and verify the analyses.

Experimental Apparatus

Figures 1 to 5 show the research hardware that will be used to run the experiments. Figure 1 is a schematic of the facility showing the orientation of the test section and the various instrumentation. Figure 2 is a side-view photograph of the test section where flow is from left to right. As shown in figure 3 a mixture of gaseous hydrogen and nitrogen flows in the upper duct while the lower duct carries air that can be heated to a temperature of 1100 °F. Both streams are accelerated in the nozzle to a maximum velocity of Mach 0.9. The two streams are kept separate until they mix and react in the test section. A blunt edge is provided to promote mixing of the two streams.

The test specimen for these experiments is located in the aft end of the test section as shown in figure 4 and is exposed to the products of combustion. The hot gases are finally exhausted either to atmosphere or to altitude exhaust (0.5 psia minimum).

The test section has two rectangular sapphire windows (9 in. long by 4 in. wide) on each side and smaller windows (9 in. by 1 in.) on the top and bottom. These allow the use of various photographic techniques during testing. These techniques include both high-speed and schlieren photography as well as infrared thermal imaging of the specimen surface and laser Doppler anemometry measurement of the gas stream.

Test specimen.—The test specimen and the specimen holder are shown in figure 5. The specimen holder is mounted on the sidewall and cantilevered into the gas stream. The test speci-

men is only a 1-in.-wide strip on the specimen holder in the midstream location. The test specimen is configured to represent a turbine airfoil leading edge. However, even more important is its location in a transition region where large thermal gradients may occur. The first test material will be Haynes 188 superalloy. This material was selected to provide a state-of-the-art baseline that will be used as a reference when developing the analysis techniques and interpreting the results. The initial wall thickness of the test specimens will be 0.025 in.

Attaching the test specimens to the holder is a challenging task because of the differentials in thermal expansion. In addition, the type of edge restraint is important to the structural analysis of the specimen. The analysis is greatly simplified by selecting a material with isotropic properties. In the future the anisotropic behavior of composite materials will also be investigated.

Specimen holder.—The material used to fabricate the specimen holder must be compatible with the specimen. This means that they must be capable of being joined (by brazing or welding) as well as have similar coefficients of thermal expansion. Table I lists some compatible pairs of specimen and holder materials; their coefficients of thermal expansion and thermal conductivities are plotted in figures 6 and 7.

A significant problem is getting acceptable braze joints for the ceramic specimens. The technology of brazing ceramics was developed by the electronics industry (refs. 2 to 4), but until recently not much emphasis has been placed on mechanical strength and structural integrity. This is a critical area where additional research is needed.

Instrumentation

Extensive and sophisticated instrumentation is available with which to determine the boundary conditions and the environment for the test specimens. These include laser Doppler anemometers (LDA) and infrared thermal imaging systems. In addition, conventional temperature and pressure instrumentation is available. The various instrumentation systems are discussed here.

LDA.—A two-component (four beam) LDA system will be used to make point measurements of the time-evolved velocity inside the flow field over the test specimen. In order to obtain a high-intensity scattered signal for high signal-to-noise ratio, a 3.75× beam expander and forward scattering will be used.

IR thermal imager.—An infrared thermal imaging system is available to provide both a thermal map of the specimen surface temperature and a distribution of the surface heat transfer rate. The surface temperature distribution is mapped by a scanning optical pyrometer that can provide 30 images of the specimen per second. The accuracy of the overall system depends on many factors, including the effect of

windows, intervening gases, and the surface emissivity. However, it is anticipated that temperatures can be determined to within 1 percent of the actual values.

By switching the camera system to a line-scan mode, the heat transfer rate can be determined from the time response of the surface temperature to a harmonic change in the free-stream temperature. This is accomplished by assuming that the surface can be modeled by a semi-infinite solid. Then the time response of the surface temperature to a perturbation in the free-stream temperature can be used to determine the heat transfer coefficient.

Total temperature.—The mean and fluctuating components of the free-stream total temperature will be measured with a fiber optic temperature probe. Temperatures up to 3200 °F and 1000 Hz can be measured by this system. Traversing the free stream in the plane of the test-specimen leading edge will provide the temperature profile of the fluid approaching the specimen.

Conventional instrumentation.—The static free-stream pressure distribution over the specimen and the coolant inlet and exit pressures will be measured by conventional pressure transducers. Specimen reference temperatures will be measured by embedded thermocouples. The coolant inlet and exit temperatures will be measured by swaged, open-ball thermocouples. The coolant flow rate will be measured by a standard orifice flowmeter.

Thermal Analysis

Thermal analyses discussed herein were made to determine the temperature distribution and gradients in the test specimen and the specimen holder, to develop analysis techniques, to aid in materials research, and to assist in verifying the strut design. The critical areas of interest for these analyses were the leading edge and the braze joint.

Cooling-air passages in the specimen holder were defined by parallel fins or ribs on the base strut. The skin was attached by brazing it to this part of the structure. The leading edge was the location where the temperature was highest and where the difference in thermal expansion resulted in maximum strain. It was not obvious whether attaching the skin to the rib at the leading edge would reduce the plastic strain by cooling the skin or would result in higher plastic strain because of the large temperature gradient. In order to answer this question, two models of the forward portion of the strut were generated. The first model (hereinafter referred to as model 1) incorporates a section of the test specimen, the specimen holder, and the braze joint where the rib stops before extending into the leading-edge region (see fig. 8). The other model (model 2) incorporates a section of the specimen holder where the rib wraps around the leading edge, away from the test specimen (see fig. 9).

The analyses used commercial codes where possible, with separate routines being written that interfaced with the com-

mercial codes as necessary. The following steps were taken to obtain accurate thermal results and to facilitate the use of these results in the subsequent stress analysis:

(1) The geometry and mesh for both the thermal and stress analyses were generated.

(2) The aerothermal heat fluxes on the strut surface exposed to the hot gas were determined and applied as boundary conditions in the model.

(3) The flow-field characteristics in the cooling channels were calculated and applied as boundary conditions in the model.

(4) The thermal results were transferred to the structural model as input to determine thermal stresses.

Model generation.—PATRAN (from PDA Engineering) was used as a pre- and postprocessor to generate the mesh and to display results, and the same finite element mesh was used for both the thermal and stress analyses. PATSIN (also from PDA Engineering) was used with the model data base to create a finite difference input file for SINDA (the thermal analyzer from Network Analysis Associates). The finite element meshes were generated with uniform hexagonal elements to obtain accurate conductors after translation to the SINDA input files. The finite element meshes for both models are shown in figures 8(b) and 9(b).

Aerothermal boundary conditions.—The aerothermodynamic loading was determined by using a two-dimensional Navier-Stokes code developed for flow over turbine airfoils. The output of this code gives both the static pressure distribution and the heat transfer coefficient distribution over the test specimen. The resulting heat transfer coefficients are shown in figure 10. Subroutines were written that use the geometry in the PATRAN neutral file to calculate the location and area associated with each SINDA node on the exterior of the skin; this geometric information, the free-stream combustion temperature, and the heat transfer coefficients from figure 10 were then used to apply convection boundary conditions in the form of conductors to the SINDA model.

Coolant boundary conditions.—Subroutines were written to determine the flow-field characteristics in the cooling channels, which were then applied to the SINDA model as boundary conditions. The coolant channel was broken up into discrete sections with the same number of fluid nodes along the channel as there were surface nodes in the flow direction. There was then a known channel geometry at each fluid node that could be obtained from the PATRAN data base. Starting at the supply manifold, the flow field characteristics were calculated by marching downstream and solving the conservation equations at each fluid node. One-dimensional, mixed, compressible, steady flow of an ideal gas was assumed, and the upstream conditions, the channel geometry, and the wall temperatures passed in from the SINDA model were used.

A critical area in the analysis was the accuracy of the Nusselt number correlation used in the coolant channels. The following correlation was used; it accounted for entrance effects, channel curvature, and large temperature differences

between the wall and the coolant (refs. 5 and 6):

$$Nu = 0.025 K(\theta) (Re)^{0.8} (Pr)^{0.4} T_r^n L^* \quad (1)$$

where $K(\theta)$ is a function of channel curvature, Re is the Reynolds number, Pr is the Prandtl number,

$$T_r^n = (T_w/T_b)^{0.5}$$

and

$$L^* = 1 + 0.3(x/D_h)^{-0.7}$$

where T_w is the channel wall temperature, T_b is the fluid bulk temperature, x is the distance downstream from the supply manifold, and D_h is the hydraulic diameter of the channel at x .

SINDA heat transfer analysis.—The SINDA models were set up to use files and routines that calculate and apply the boundary conditions to the thermal model automatically with each change in material properties and coolant supply conditions. Properties for the materials of interest were stored, and data for selected materials were written into the proper SINDA array positions. With geometric information from the PATRAN neutral file, the aerothermal loads and the coolant boundary conditions were applied as film coefficients and gas temperatures in the form of conductors from the skin to the boundary nodes.

In making each model, diffusion nodes were used for the solid and arithmetic nodes on the surfaces, where boundary conditions were applied and where dissimilar materials were joined. All fluid nodes are represented in SINDA as boundary nodes. The brazing alloy properties were similar to those of Inconel MA-754; therefore the braze material was modeled as the same material as the specimen holder.

Thermal/structural interface.—The thermal results were transferred as input to the MARC finite element program for thermal stress analysis through an interface program that generates nodal temperature load cards from the SINDA temperature results file. This interface program uses the weighting factor algorithm from the SINDA to NASTRAN Interface Program (SNIP) (ref. 7), the PATRAN neutral file for geometry definition and connectivity, and the SINDA temperature results file as input to interpolate between SINDA node temperatures and finite element node temperatures. Output from the program is a file containing MARC "fixed temperature" records in a compatible format.

Stress Analysis

One goal of this analysis was to determine the stress due to the differential thermal expansion between the specimen and the holder. The high stress expected and the high temperatures could result in plastic deformation. Hence, the MARC

finite element code (from Marc Analysis Research Corporation) was selected because of its excellent capabilities in the nonlinear plastic region and in analyzing composite materials. Two steps were required before proceeding with the stress analysis. First, the PATRAN model discussed in the previous section was converted into a MARC model by using the program PATMAR (from PDA Engineering). Second, the temperatures obtained from the SINDA heat transfer analysis were transferred to the MARC model, as described in the preceding section.

The two models used for the stress analyses are shown in figure 11. Note that only half of the model shown in figure 8 (model 1) was used for the stress analysis to reduce computer memory and run-time requirements. Also in model 1 the X-Y plane at $Z=0$ was located at the braze joint between the test specimen and the holder skin and extends through the centerline of the rib. The boundary conditions imposed on both models forced all nodes in the symmetry plane cutting through the center of the rib (at $Z=0$ in figs. 11(a) and (b)) to be fixed in the Z direction. The nodes in the boundary plane at $Z=0.1475$ in. and $Z=-0.1475$ in. for model 1 and at $Z=0.1475$ in. for model 2 were all constrained so that they lie in the same plane and must remain in a plane parallel to the original plane. All nodes on the boundary plane at the back of the model (at $X=0.609$ in.) were fixed in the X direction. All nodes on the X-Z plane cutting through the centerline of the strut (at $Y=0$) were fixed in the Y direction. Only thermal loading was considered in the MARC analyses because the effect of pressure loading was found to be small. However, hand calculations based on the full specimen geometry, not just on the model region, have shown higher pressure stresses on the shell. For this reason the effect of pressure was taken into account in a separate analysis, and the results were superimposed on the MARC thermal stress analysis results.

The major limitation of the analyses was that the finite element models represented only a small segment of the overall structure. The model boundary conditions were estimated because the exact boundary conditions were not known. However, depending on the material combinations analyzed, the critical failure locations were in the leading-edge region at the braze joint between the test specimen and the holder skin, at the braze joint between the skin and the rib, or between the rib and the core. These critical locations were not close to any boundaries, thus mitigating the effects of the boundary condition inaccuracies.

Results

The research goals of this program are to simulate the aerothermal loads of advanced gas turbine engines, including the large thermal gradients and subsequent thermal stresses and strains, in candidate test specimen materials. These goals generally conflict with the design goals of preventing the

specimen holder and its braze joints from failing. High temperatures and temperature gradients exist where the heat fluxes are high, and they will be largest in materials with low thermal conductivity because of their inability to conduct heat from the hot surface through the material to the coolant. These issues must also be addressed during the design of components made from these advanced materials. Whether these components are actively cooled or not, high thermal gradients will occur at some locations within the component. And consequently high thermal stresses will be induced.

In order to maintain the integrity of the braze joint for these test specimens and holders, the temperatures must be kept low enough to retain adequate material strength, and the gradients must be controlled to limit thermal stresses while at the same time preserving the research objectives. This can be done by using materials with similar thermal expansion coefficients. The brazing material must also have similar thermal properties as the pieces being joined, must be ductile to relieve stresses, and must remain strong enough at high temperatures to withstand the internal pressure and thermal stresses. Figures 6 and 7 show a comparison of material thermal properties used in this analysis. The material properties are obtained from Inco Company literature (ref. 8), the "Aerospace Structural Metals Handbook" (ref. 9), "Thermophysical Properties of Matter" (ref. 10), and Henisch and Roy (ref. 11). All analyses assume isotropic temperature-dependent properties. For the composite materials the properties used are in the X-X plane.

Table II tabulates results for both models with the same boundary conditions on the combustion side of the strut and the same coolant air supply conditions. The coolant air supply conditions are 60 psia, 0.3 lb/sec, and 70 °F. The coolant air properties were obtained from the GASPLUS program (ref. 12). Note that a stress analysis was not done on all the material combinations listed in table II because of the long computer run times needed. The element locations referred to in table II are shown in figure 12. Element 2513 is not included in the stress model. Because of the differences in material properties the flow conditions downstream of the supply manifold vary somewhat. Figure 13 shows the coolant flow conditions for model 1 calculated for the materials with the lowest (Haynes 188 test specimen and Inconel MA-754 specimen holder) and the highest thermal conductivities (tungsten/copper test specimen and tungsten holder). The rapid change in heat transfer coefficient before and after the leading-edge region is a result of the jump in average coolant channel wall temperatures occurring where the rib stops. A three-dimensional analysis of the coolant flow would be required to more accurately calculate these values.

Figures 14 to 21 show results from model 1 for eight different material combinations. The highest temperature gradients occurred in the forward portion of the rib at the braze joint, and the highest material temperatures occurred at the leading edge. The gradients and maximum temperatures were considerably higher for the materials with low thermal conductivity, as can be seen in table II and figures 22 and 23.

The results of the stress analysis of a Haynes 188 specimen in an Inconel MA-754 specimen holder are shown in figures 14(b) and (c). The predicted maximum effective stress was over 85 000 psi at the braze joint in the leading edge. Hence, permanent plastic deformation of the structure is predicted because the yield strength of this material is 44 000 psi at the predicted temperature of 1220 °F. At this temperature the ultimate tensile strength of the Haynes 188 is 105 000 psi; therefore it is predicted that the strut will survive. The plot of the plastic deformation shows a maximum plastic deformation of 0.6 percent at the leading-edge joint, where the maximum stress is predicted. Note, also, that high stress is predicted at the locations where the test specimen and the holder skin join the rib as well as where the core joins the rib for this material combination. Small plastic deformation is predicted at the joint between the skin and the rib. The significance of the plastic deformation is that the structure may be distorted after a test to the extent that it may not be reused.

The second case (figs. 16(b) and (c)) is for a silicon carbide specimen in the same Inconel specimen holder. The maximum plastic strain was 4.5 percent at the leading-edge joint and 3.5 percent at the skin/rib joint. Because the difference in the thermal expansion was larger than in the previous situation, the stresses, and even more significantly the plastic strain, increased.

Figures 17(b) and (c) show the results of modeling a tungsten specimen brazed to an Inconel MA-754 specimen holder. The maximum plastic strain was 3.6 percent at the leading-edge joint (not visible). At the skin/rib joint the plastic strain was almost 3 percent.

The stress analysis of a tungsten/copper composite material attached to an Inconel MA-754 holder is shown in figures 18(b) and (c). Because of the higher yield strength of this material the maximum plastic deformation was limited to 1.9 percent.

The results of modeling a tungsten/copper composite test specimen and a tungsten holder are shown in figures 20(b) and (c). Here the coefficients of thermal expansion are far enough apart that a maximum plastic strain of 2.9 percent was predicted. This is even higher than the 1.9 percent predicted for the tungsten/copper and Inconel MA-754 combination discussed previously. This amount of plastic deformation will probably result in unacceptable distortion of the structure after the first test. A better match of the thermal expansion coefficients is needed to reduce the permanent plastic deformation noted in the previous examples. For ceramics such as silicon carbide, good choices are tungsten and other refractory metals as shown figure 6. These materials are strong and readily available and can be manufactured into complex structures. However, two deficiencies in their performance are their tendency to oxidize into a vapor and brittleness at room temperature. The first problem can be overcome by coatings, and the second by proper design. The silicon carbide test specimen and tungsten holder results are shown in figure 21(b). Note that the stress is now less than the yield strength of both alloys and that no plastic strain was predicted.

Results for model 2 are shown in figure 24 for an Inconel MA-754 holder skin and core. The coolant supply conditions (air at 60 psia, 0.3 lb/sec, and 70 °F) were the same as those used in the model 1 analyses. The thermal analysis was run for a 3000 °F combustion temperature (fig. 24(a)) and for a 4000 °F combustion temperature (fig. 24(b)). The stress analysis was run only on the 4000 °F case (figs. 24(c) and (d)). The maximum plastic strain was 1.3 percent. This is a significant increase from the results shown in figure 14(c); however, the combustion temperature is higher in model 2.

Figures 25 to 29 show results from model 2 for five additional material combinations, a combustion temperature of 3000 °F, and the same coolant supply conditions as those for figure 24. As shown in table II the highest gradients occur where the skin attaches to the rib at the leading edge. The maximum temperatures and gradients are somewhat lower in this portion of the strut because the coolant channel is narrower (0.243 in. in model 2 compared with 0.4 in. under the test specimen in model 1) and the rib is thinner (0.05 in. in model 2 compared with 0.15 in. in model 1). The difference between the two rib geometries can be seen by comparing the results shown in figures 27(b) and (c) with figures 17(b) and (c). The rib extending around the leading edge drastically increased the plastic strain from 3.6 percent to 12.3 percent, making this material combination and geometry unacceptable.

Concluding Remarks

On the basis of the analytical results the Haynes 188 test specimen and the Inconel MA-754 specimen holder baseline design will survive testing. The 0.6-percent plastic deformation predicted is small, and the warpage may be small enough to allow the specimen holder to be brazed to a second test specimen. However, brazing the other candidates for test materials to the Inconel specimen holder will result in much higher plastic strains. Warpage after use with a second material will be significant, making the use of the Inconel holder with a third test piece improbable.

When additional struts are made, in order to test materials such as silicon carbide and tungsten/copper composites, the specimen holder should be made of a material with a better match of thermal expansion coefficients. Tungsten is the recommended material for the new test specimen holders. When matched with the silicon carbide test specimen, the tungsten holder exhibits no plastic strain and could be reused for additional test materials. A tungsten/copper composite will probably survive being tested with a tungsten holder, but it should

be the last material combination tested because even the tungsten strut will suffer unacceptable distortion.

The results show a much higher plastic strain when the rib wraps around the leading edge as it does in model 2. Large temperature gradients occur at the location of maximum temperature on the leading edge. Therefore, the rib should stop before it extends around the leading edge under the test specimen to avoid the joining of dissimilar materials in this critical area. If possible, the rib should not wrap around the leading edge in the remainder of the strut either because of the 1.3-percent plastic strain predicted when using the baseline configuration of Inconel MA-754. However, this design may be necessary to give additional strength to withstand the higher coolant pressures inside the strut.

Lewis Research Center,
National Aeronautics and Space Administration,
Cleveland, Ohio, July 12, 1991

References

1. Simoneau, R.J.; and Hudson, D.A.: CFD in the Context of IHPTET—The Integrated High Performance Turbine Technology Program. AIAA Paper 89-2904, July 1989. (Also, NASA TM-102132.)
2. Phillips, W.M.: Metal-to-Ceramic Seals for Thermionic Converters—A Literature Survey. NASA CR-108231, 1969.
3. Clarke, J.F.; Girard, E.H.; and Ritz, J.W.: State-of-the-Art Review of Ceramic-to-Metal Joining. AFML-TR-65-143, Air Force Materials Laboratory, Wright Patterson AFB, OH, 1965. (Avail. NTIS, AD-465809.)
4. Nichols, M.G.; and Mortimer, D.A.: Ceramic/Metal Joining for Structural Applications. *Mater. Sci. Technol.*, vol.1, no. 9, Sept. 1985, pp. 657-665.
5. Hendricks, R.C.; and Simon, E.F.: Heat Transfer to Hydrogen Flowing in a Curved Tube. *Multiphase Flow Symposium*, N.J. Lipstein, ed., ASME, 1963, pp. 90-93.
6. Hendricks, R.C., et al.: Bulk Expansion Factors and Density Fluctuations in Heat and Mass Transfer. 15th International Congress of Refrigeration, Venezia, Sept. 23-29, 1979, Vol. 2, paper B1-119.
7. Winegar, S.R.: SINDA-NASTRAN Interfacing Program—Theoretical Description and User's Manual. NASA TM-100158, 1987.
8. High Temperature High Strength Nickel Base Alloys. The International Nickel Company, Inc., 3rd Edition, July 1977.
9. Aerospace Structural Metals Handbook. Battelle Columbus Laboratories, Columbus, OH, 1967.
10. Touloukian, Y.S., ed.: Thermophysical Properties of Matter, Vol. 1, Conductivity: Metallic Elements and Alloys. Plenum, 1970.
11. Henisch, H.K.; and Roy, R.: Silicon Carbide—1968. Pergamon Press, 1969. (Also published as a special issue of Materials Research Bulletin.)
12. Fowler, J.R.: GASPLUS User's Manual. Wright Patterson AFB, OH, 1988.

TABLE I.—COMPATIBLE SPECIMEN AND
HOLDER MATERIALS

Specimen	Holder
Haynes 188 Silicon carbide Copper/tungsten	Inconel Tungsten Tungsten

TABLE II.—SUMMARY OF THERMAL AND STRESS ANALYSES FOR MODELS 1 AND 2

(a) Model 1

Material combination (specimen/holder)	Leading edge (element 2513)		Forward skin/rib interface (element 2285)				Braze joint at leading edge (element 281)			
	Tempera- ture, °F	Gradient, °F/in.	Tempera- ture, °F	Gradient, °F/in.	Stress, psi	Strain, percent	Tempera- ture, °F	Gradient, °F/in.	Stress, psi	Strain, percent
Haynes 188/MA-754	1220	2749	743	7258	52 549	---	1179	417	44 568	0.6
MA-754/MA-754	1195	2378	728	6309	-----	---	1164	78	-----	---
Silicon carbide/MA-754	1140	1934	762	6590	97 379	3.5	1138	540	99 851	4.5
Tungsten/MA-754	969	567	814	6478	78 579	3.6	1030	2345	80 827	---
Tungsten/copper/MA-754	881	206	818	5916	-----	---	953	3180	-----	1.9
Tungsten/copper/ silicon carbide	855	210	783	4303	-----	---	909	2206	-----	---
Tungsten/copper/tungsten	823	216	740	1898	88 438	2.9	837	511	156 679	---
Silicon carbide/tungsten	1106	1931	688	5741	15 230	---	939	1731	48 395	---

(b) Model 2

Material combination (specimen/holder)	Leading edge at midchannel (element 1)				Leading edge skin/rib interface (element 783)				Leading edge above rib (element 617)			
	Tempera- ture, °F	Gradient, °F/in.	Stress, psi	Strain, percent	Tempera- ture, °F	Gradient, °F/in.	Stress, psi	Strain, percent	Tempera- ture, °F	Gradient, °F/in.	Stress, psi	Strain, percent
Haynes 188/MA-754	1132	3009	-----	---	926	6547	-----	---	1004	3425	-----	---
MA-754/MA-754	1144	2516	-----	---	962	6049	-----	---	1027	2868	-----	1.3
Silicon carbide/ MA-754	1017	1984	-----	---	896	4994	-----	---	939	2029	-----	---
Tungsten/MA-754	877	587	218 532	---	845	3349	214 959	12.3	857	592	310 007	---
Tungsten/copper/ MA-754	801	220	-----	---	790	2758	-----	---	795	221	-----	---
Tungsten/tungsten	779	608	25 019	---	717	1578	7 138	---	731	618	34 497	---

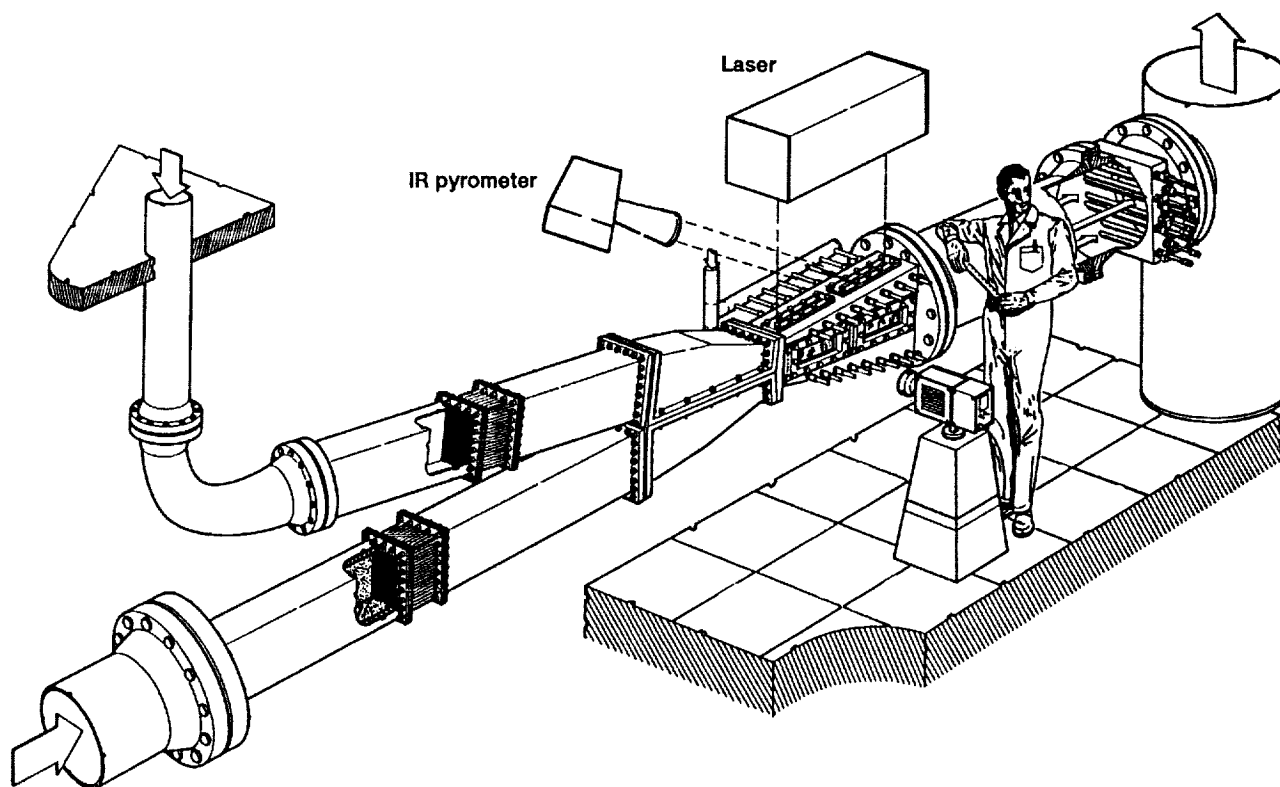


Figure 1.—Schematic of aerothermal loads experiment facility.

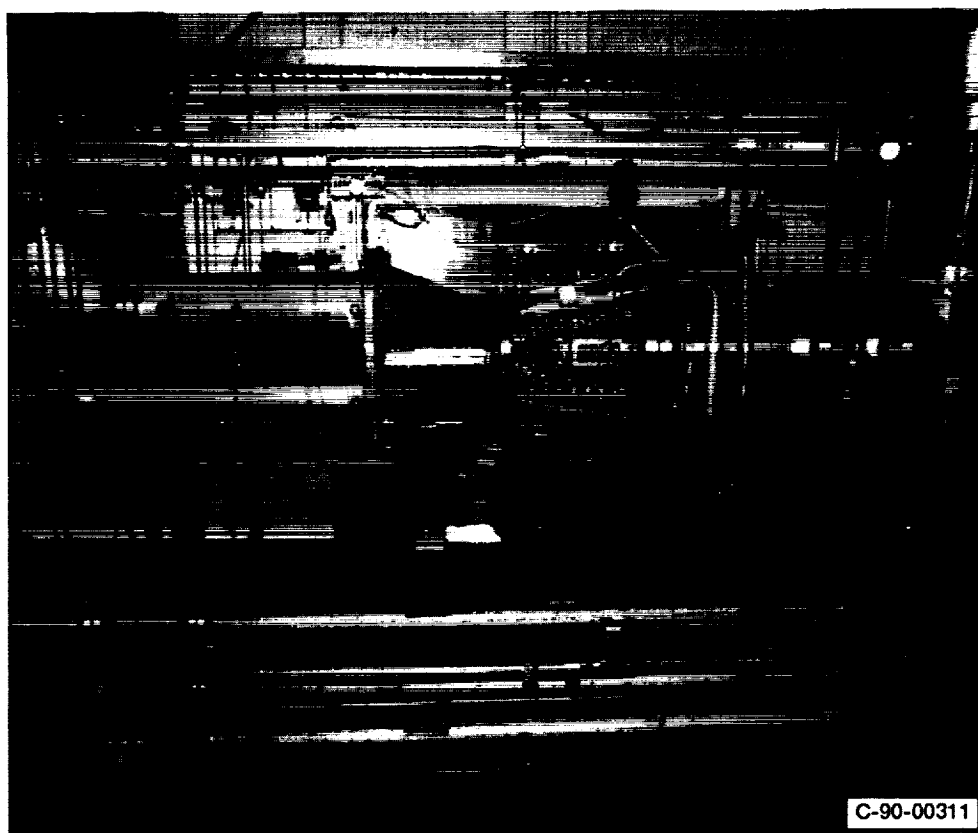


Figure 2.—Aerothermal loads experiment facility.

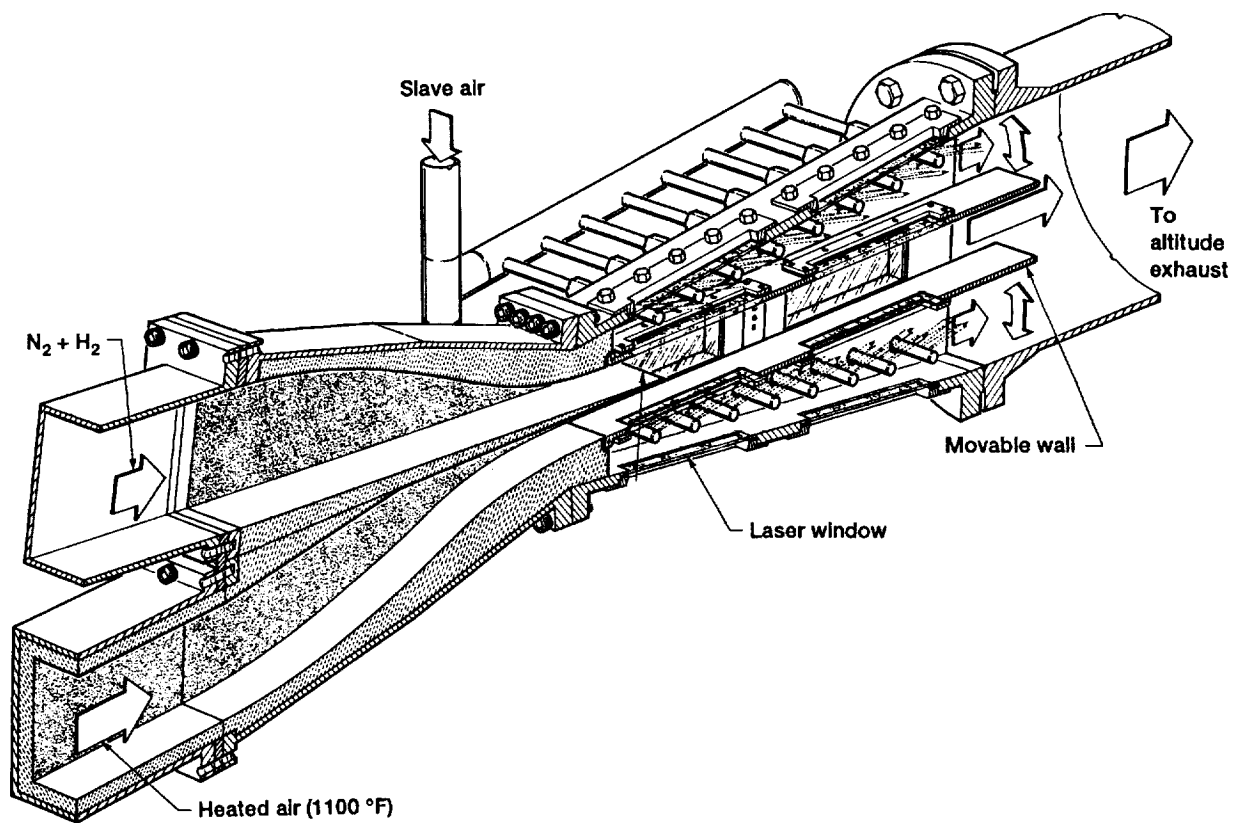


Figure 3.—Schematic of facility test section.

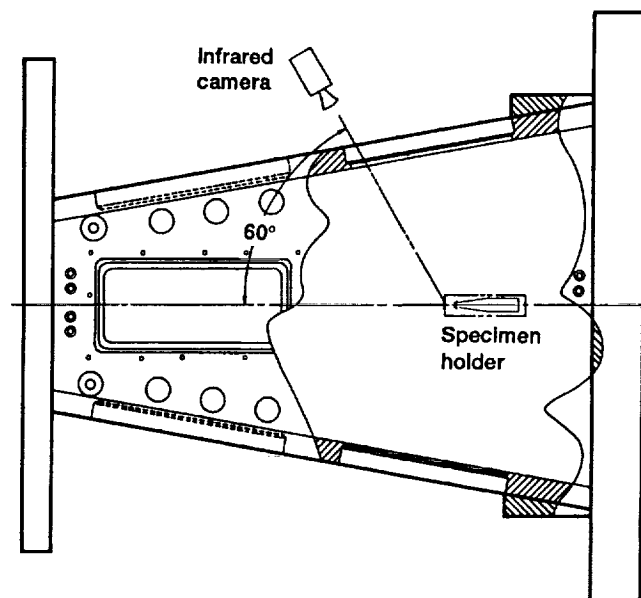


Figure 4.—Specimen holder installation in test section.

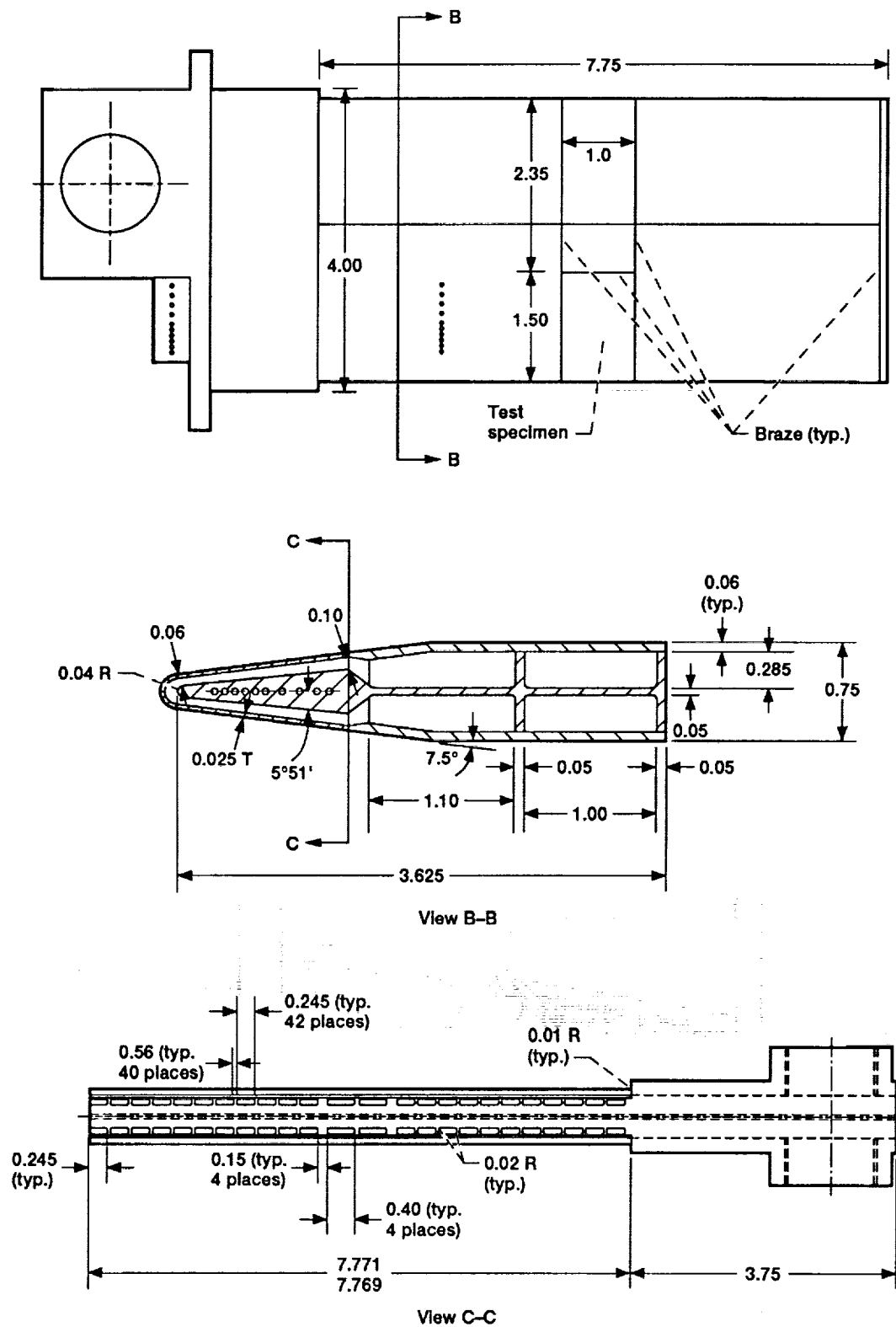


Figure 5.—Details of test specimen and specimen holder.

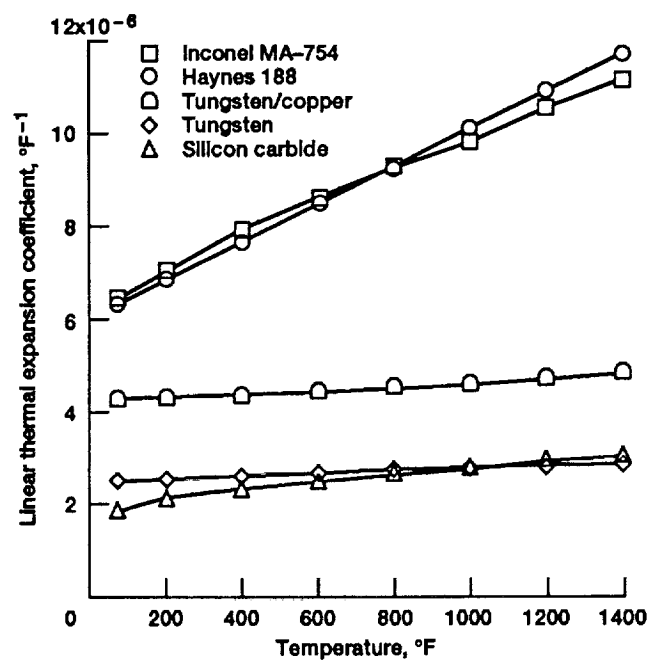


Figure 6.—Coefficients of thermal expansion for specimen and holder materials.

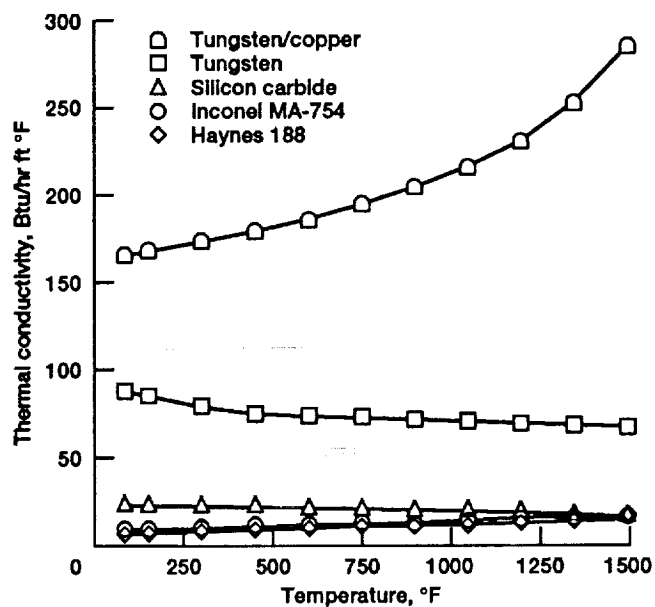
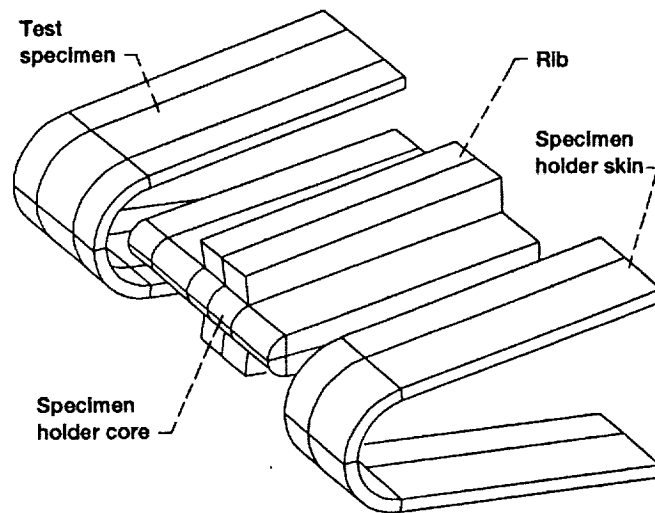
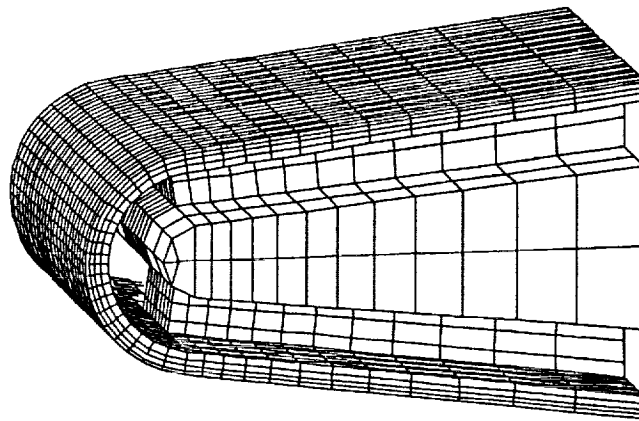


Figure 7.—Thermal conductivities for specimen and holder materials.

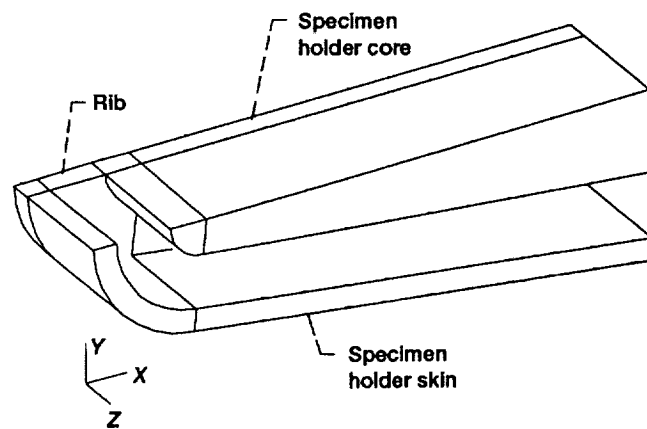


(a) Geometry.

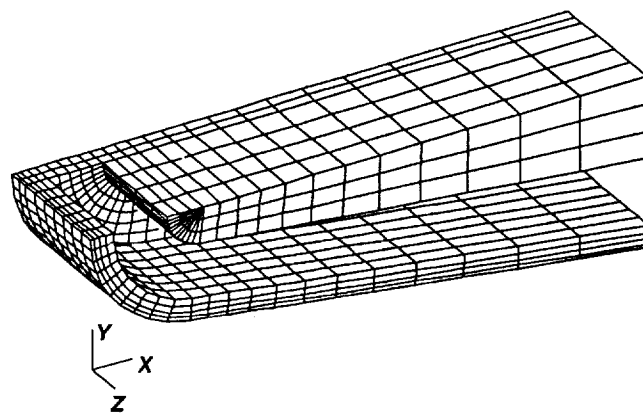


(b) Mesh.

Figure 8.—Model 1 of forward portion of strut.



(a) Geometry.



(b) Mesh.

Figure 9.—Model 2 of forward portion of strut.

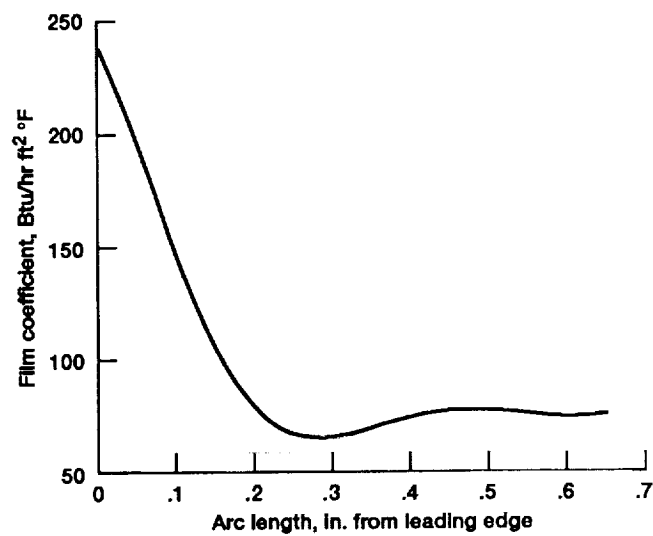
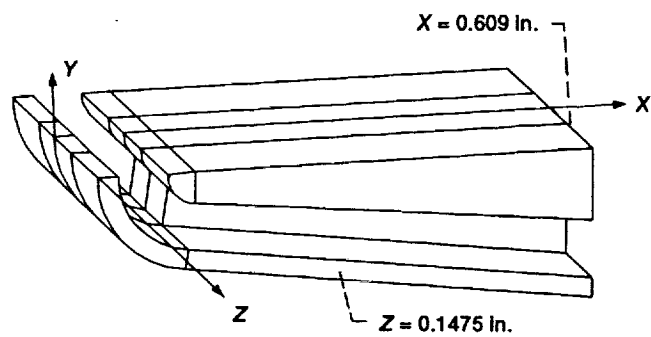
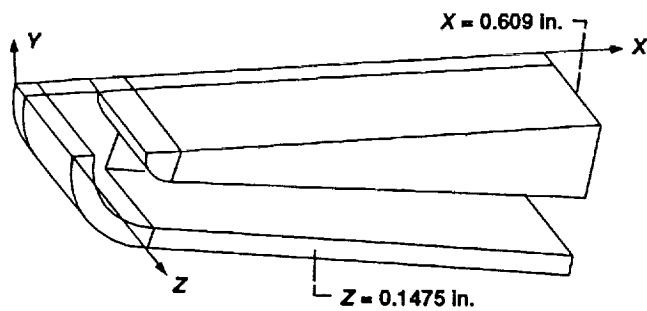


Figure 10.—Aerothermal loading.

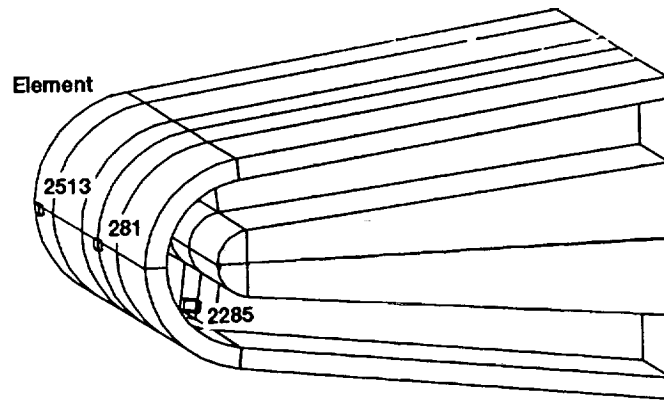


(a) Model 1.

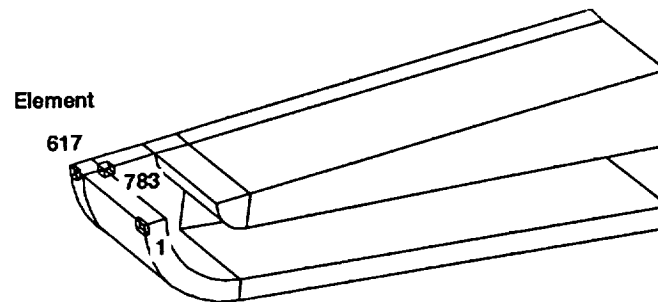


(b) Model 2.

Figure 11.—Models used for stress analysis.



(a) Model 1.



(b) Model 2.

Figure 12.—Element locations. (See table II.)

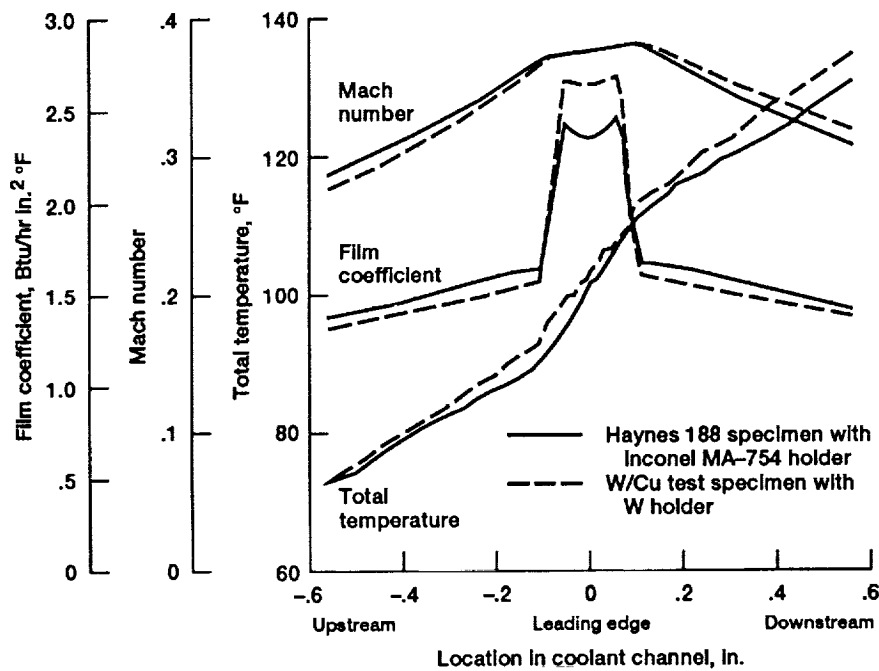
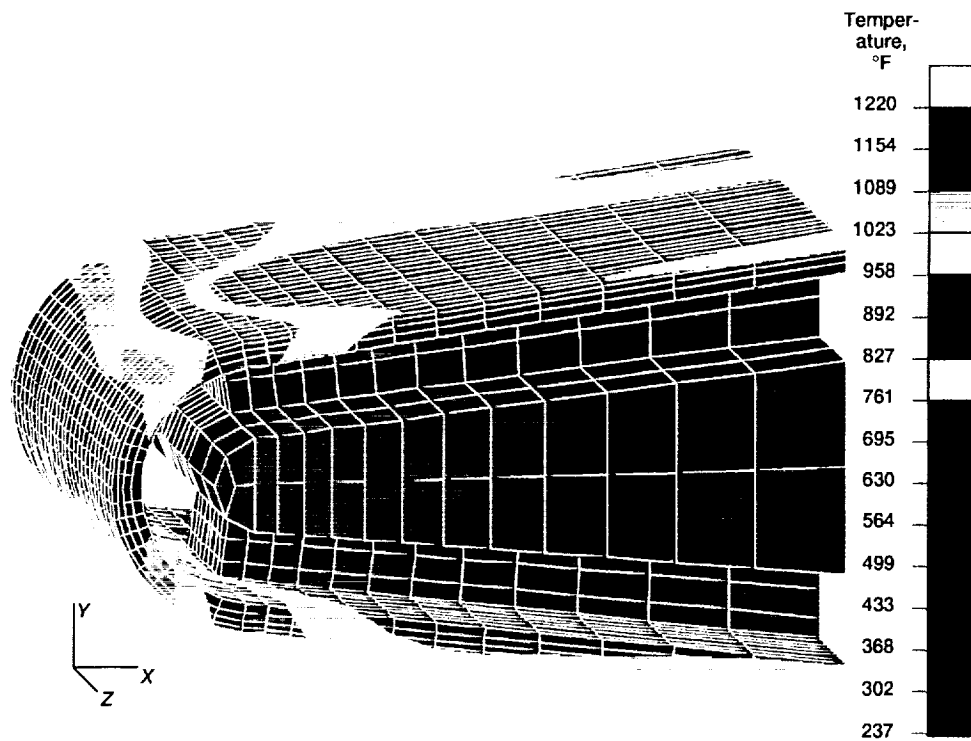
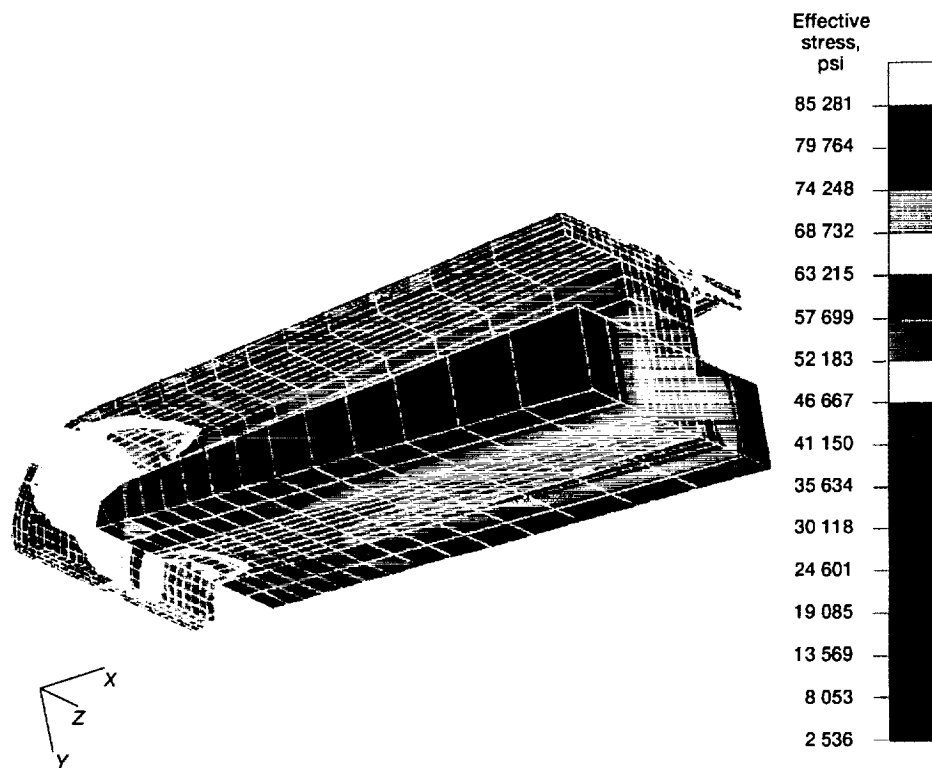


Figure 13.—Calculated flow conditions in coolant channel for material combination with highest (tungsten/copper test specimen and tungsten holder) and lowest (Haynes 188 test specimen and Inconel MA-754 holder) thermal conductivities.



(a) Temperature distribution.



(b) Stress distribution.

Figure 14.—Model I analysis of Haynes 188 test specimen and Inconel MA-754 holder. Combustion temperature, 3000 °F. Coolant supply conditions: flow rate, 0.3 lb/sec; pressure, 60 psia; temperature, 70 °F.

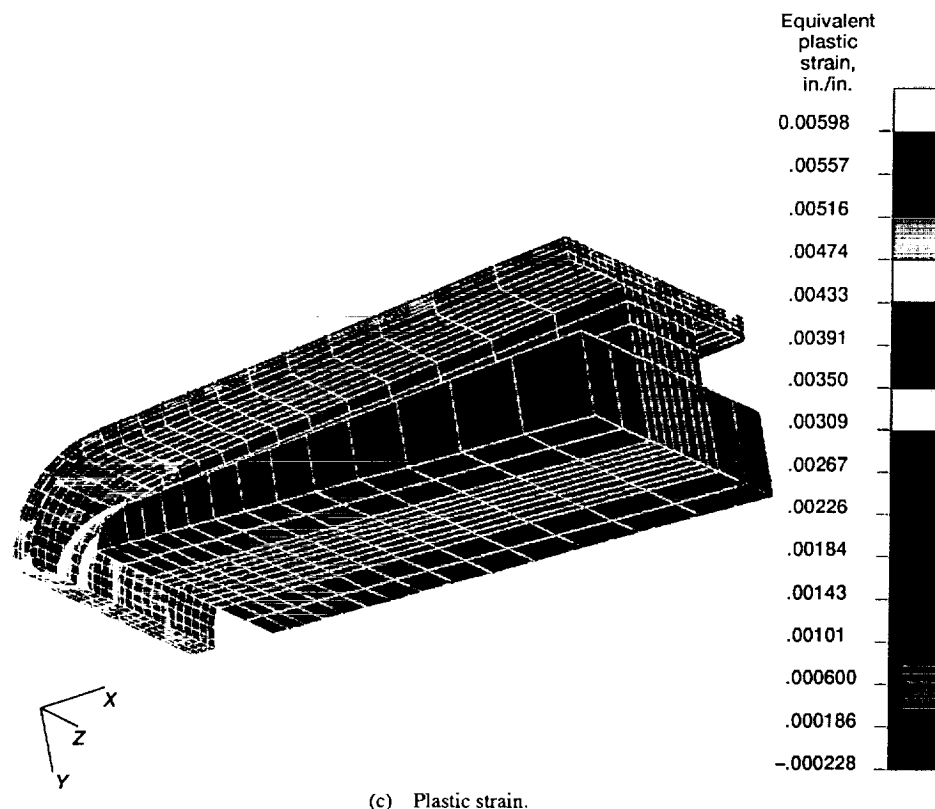


Figure 14.—Concluded.

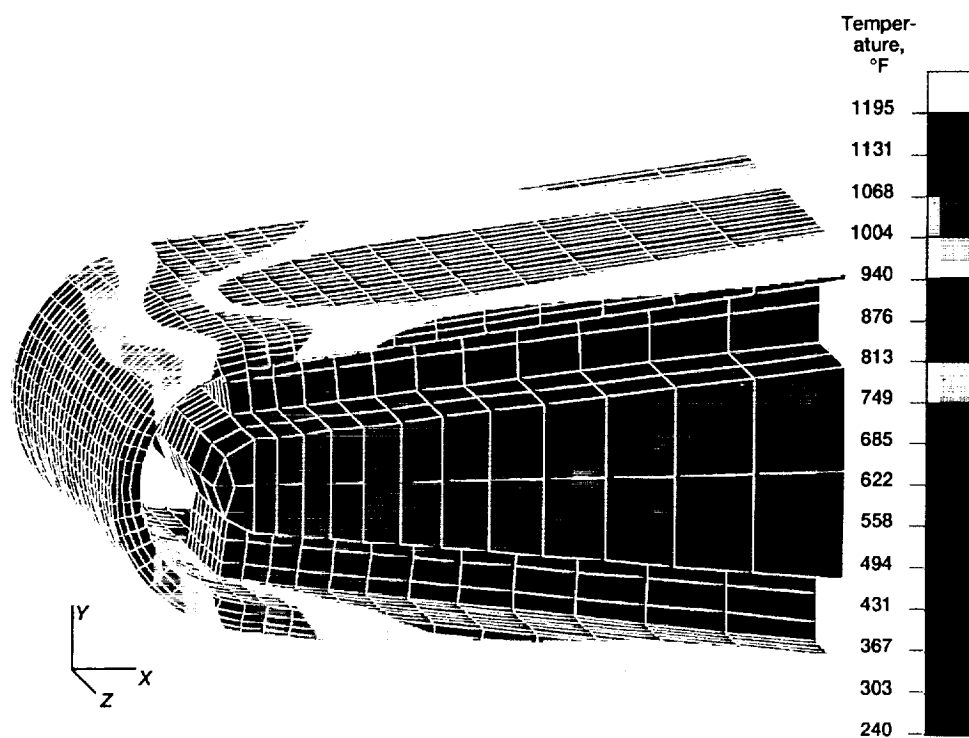
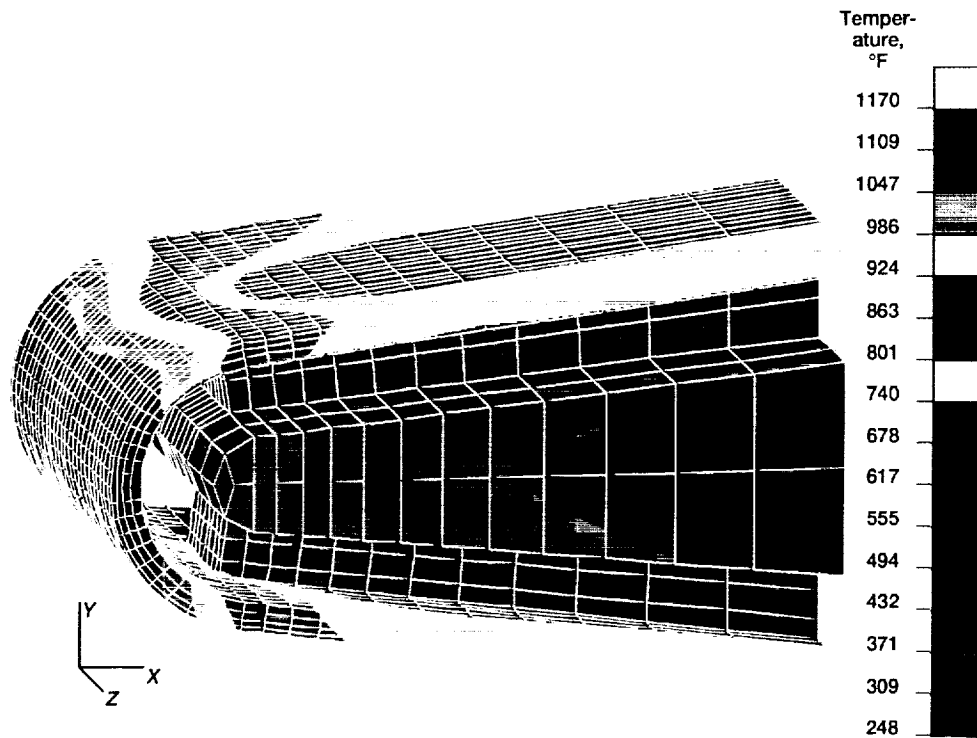
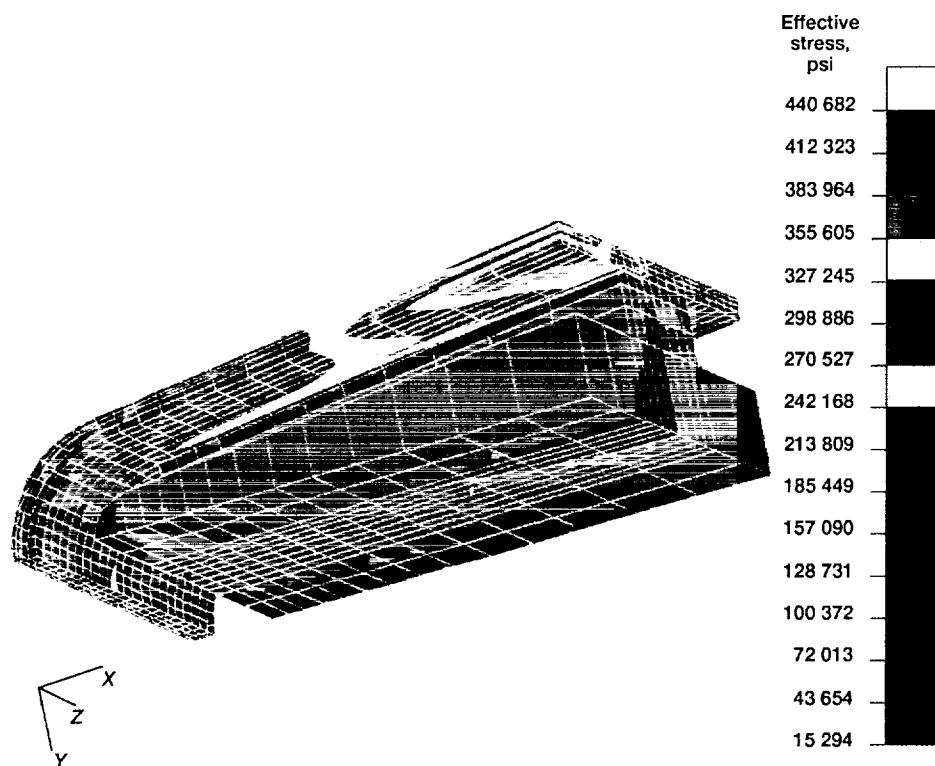


Figure 15.—Model 1 temperature distribution of Inconel MA-754 test specimen and Inconel MA-754 holder. Combustion temperature, 3000 °F. Coolant supply conditions: flow rate, 0.3 lb/sec; pressure, 60 psia; temperature, 70 °F.



(a) Temperature distribution.



(b) Stress distribution.

Figure 16.—Model I analysis of silicon carbide test specimen and Inconel MA-754 holder. Combustion temperature, 3000 °F. Coolant supply conditions: flow rate, 0.3 lb/sec; pressure, 60 psia; temperature, 70 °F.

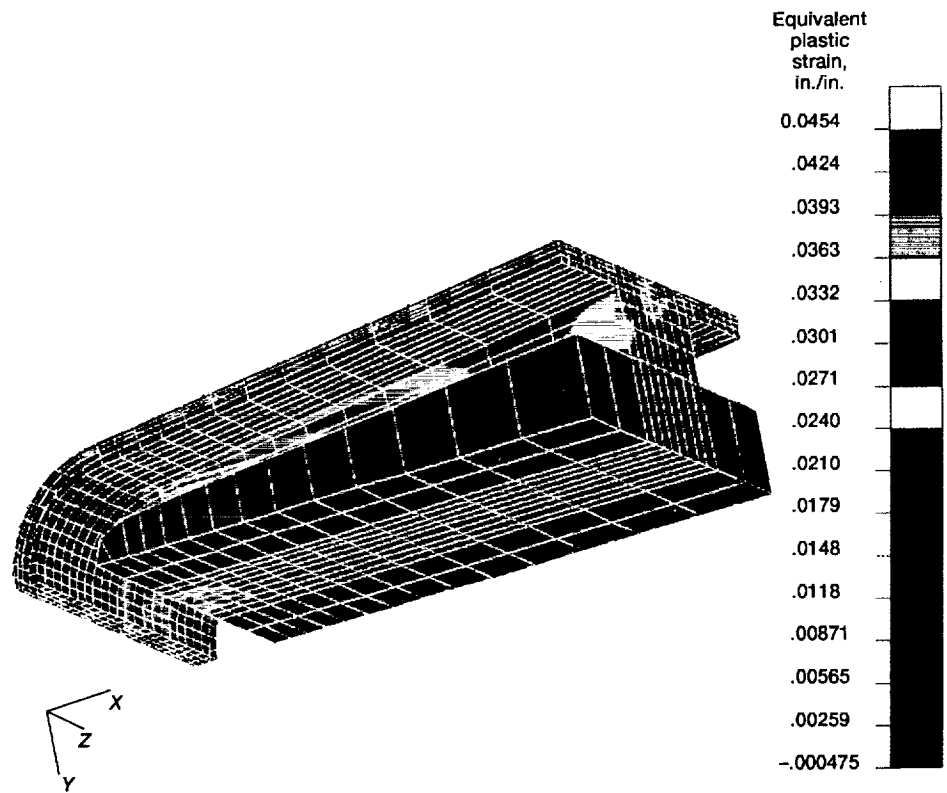


Figure 16.—Concluded.

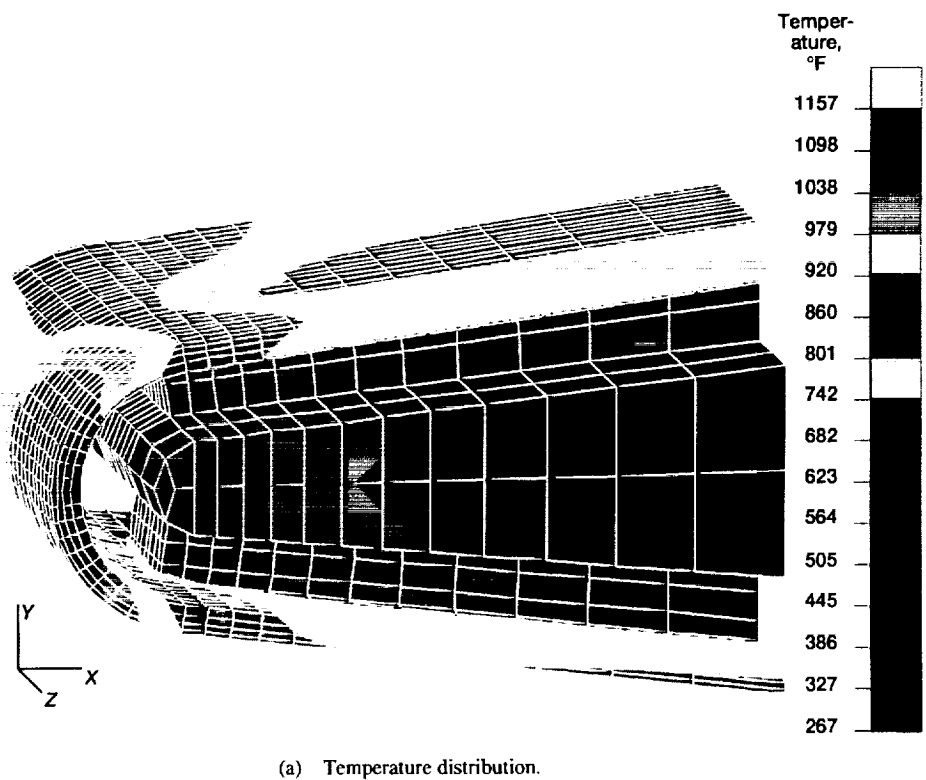


Figure 17.—Model 1 analysis of tungsten test specimen and Inconel MA-754 holder. Combustion temperature, 3000 °F. Coolant supply conditions: flow rate, 0.3 lb/sec; pressure, 60 psia; temperature, 70 °F.



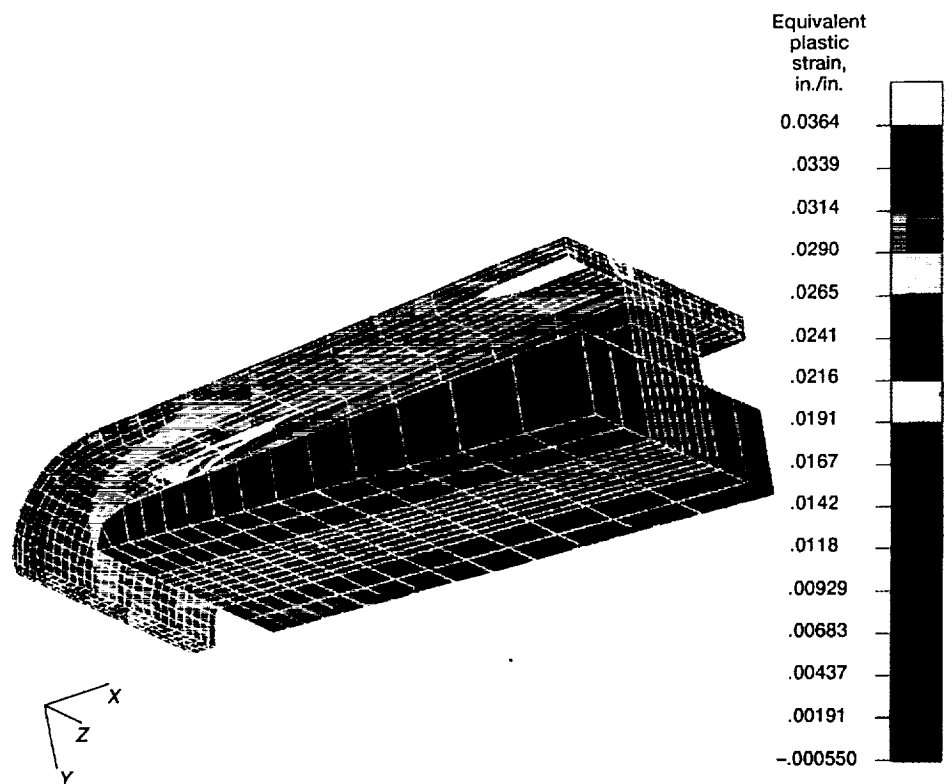
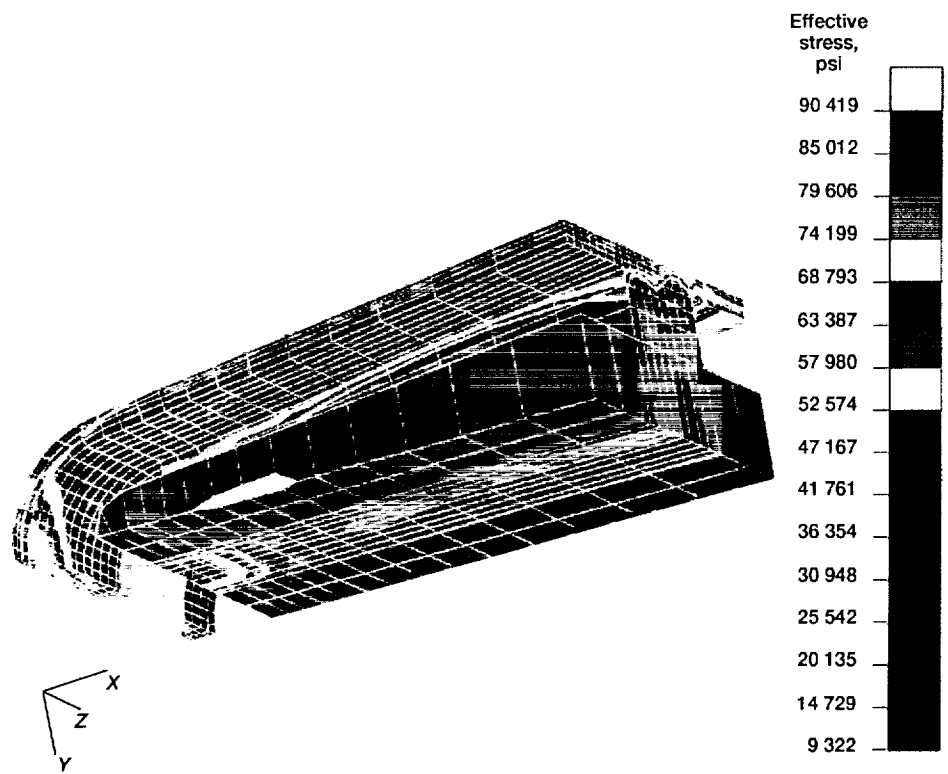
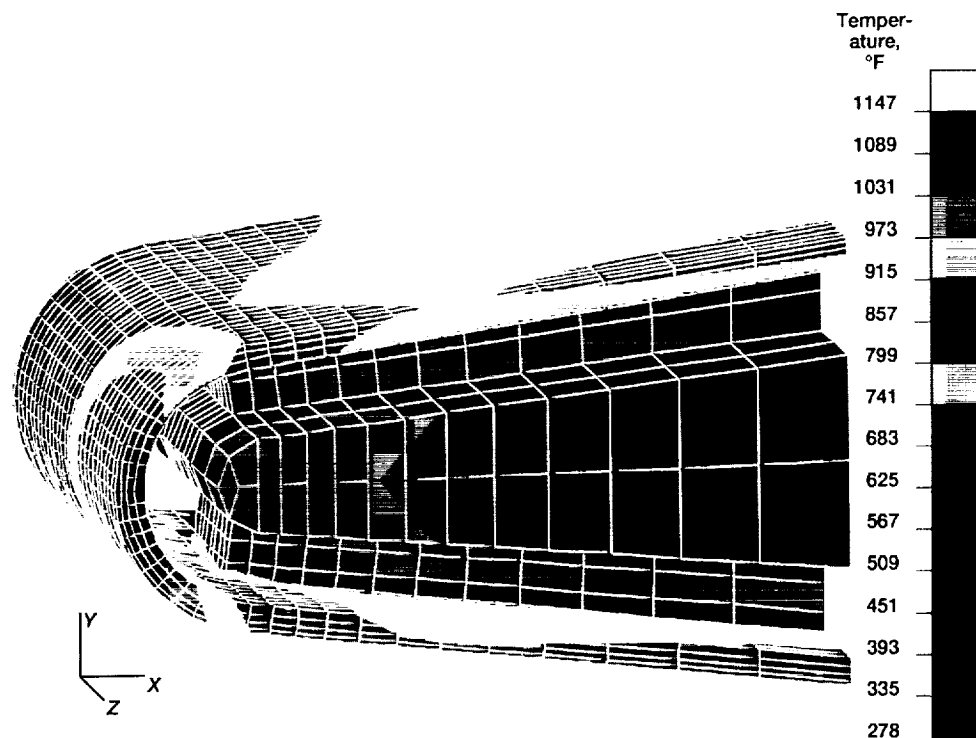
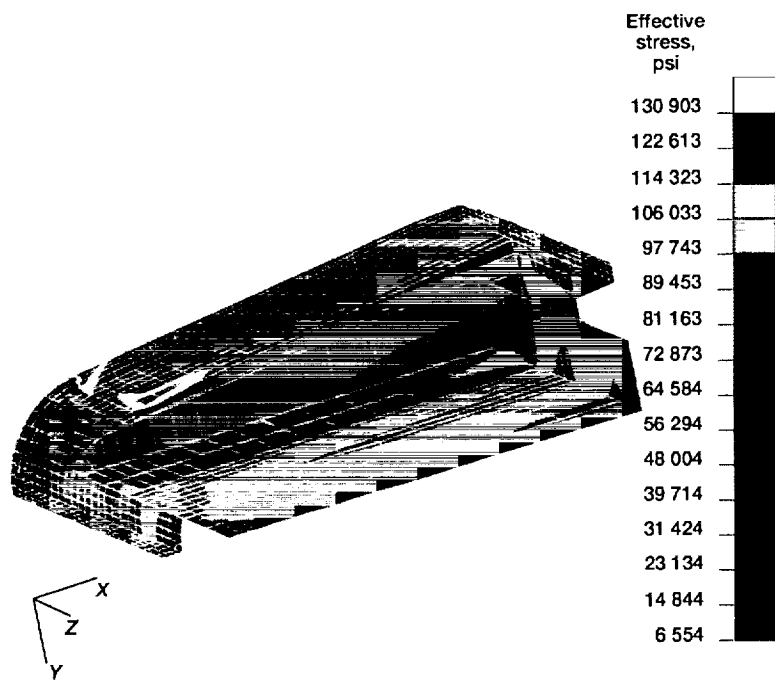


Figure 17.—Concluded.



(a) Temperature distribution.



(b) Stress distribution.

Figure 18.—Model 1 analysis of tungsten/copper test specimen and Inconel MA-754 holder. Combustion temperature, 3000 °F. Coolant supply conditions: flow rate, 0.3 lb/sec; pressure, 60 psia; temperature, 70 °F.

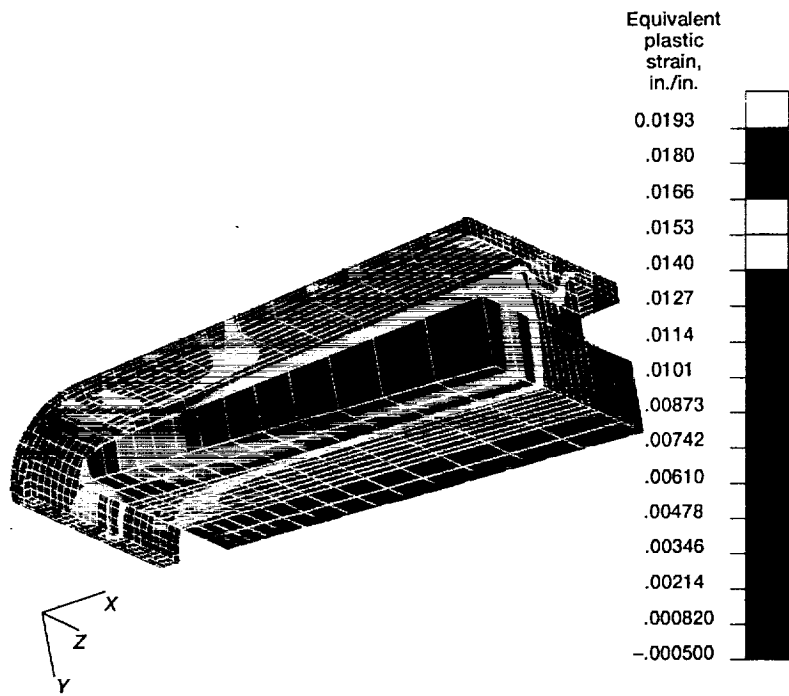


Figure 18.—Concluded.

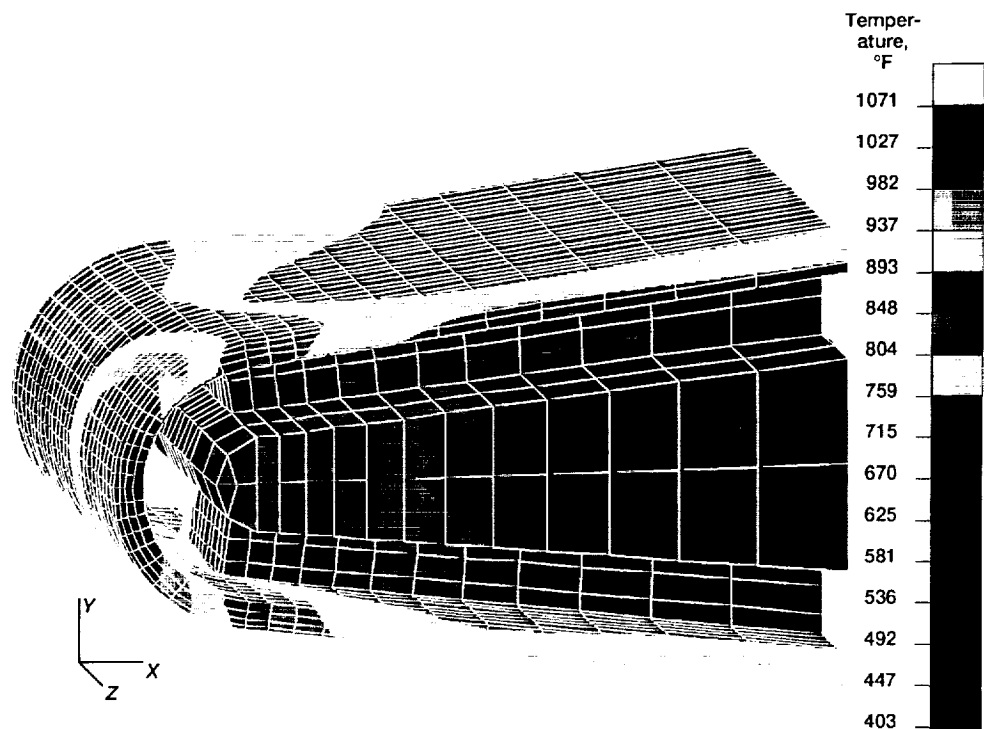
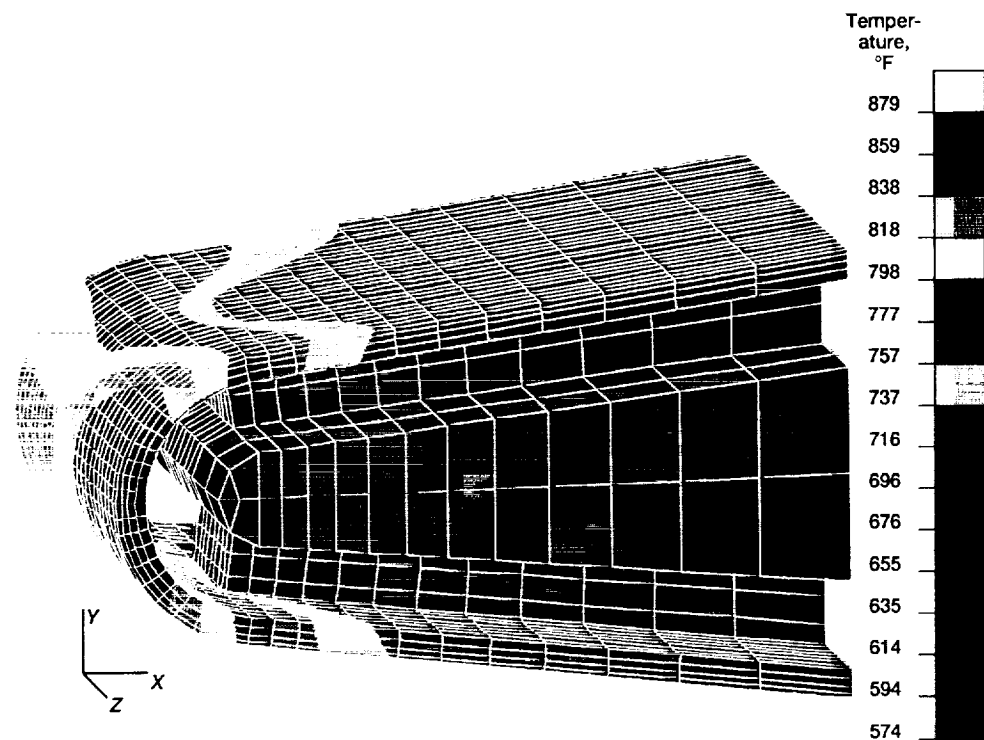
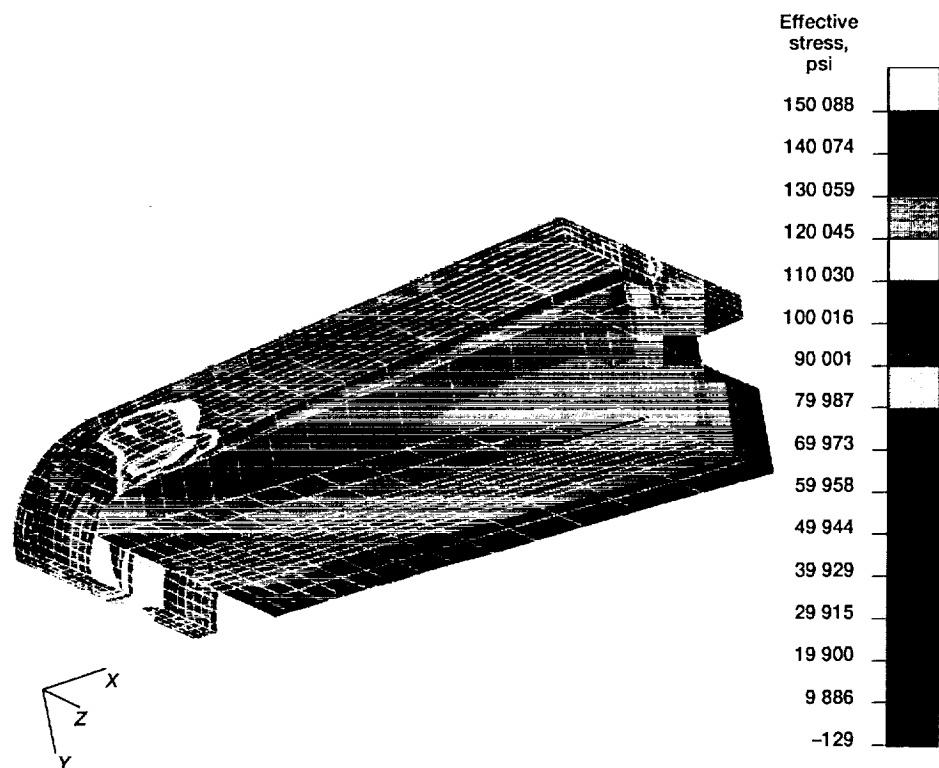


Figure 19.—Model 1 temperature distribution of tungsten/copper test specimen and silicon carbide holder. Combustion temperature, 3000 °F. Coolant supply conditions: flow rate, 0.3 lb/sec; pressure, 60 psia; temperature, 70 °F.



(a) Temperature distribution.



(b) Stress distribution.

Figure 20.—Model 1 analysis of tungsten/copper test specimen and tungsten holder. Combustion temperature, 3000 °F. Coolant supply conditions: flow rate, 0.3 lb/sec; pressure, 60 psia; temperature, 70 °F.

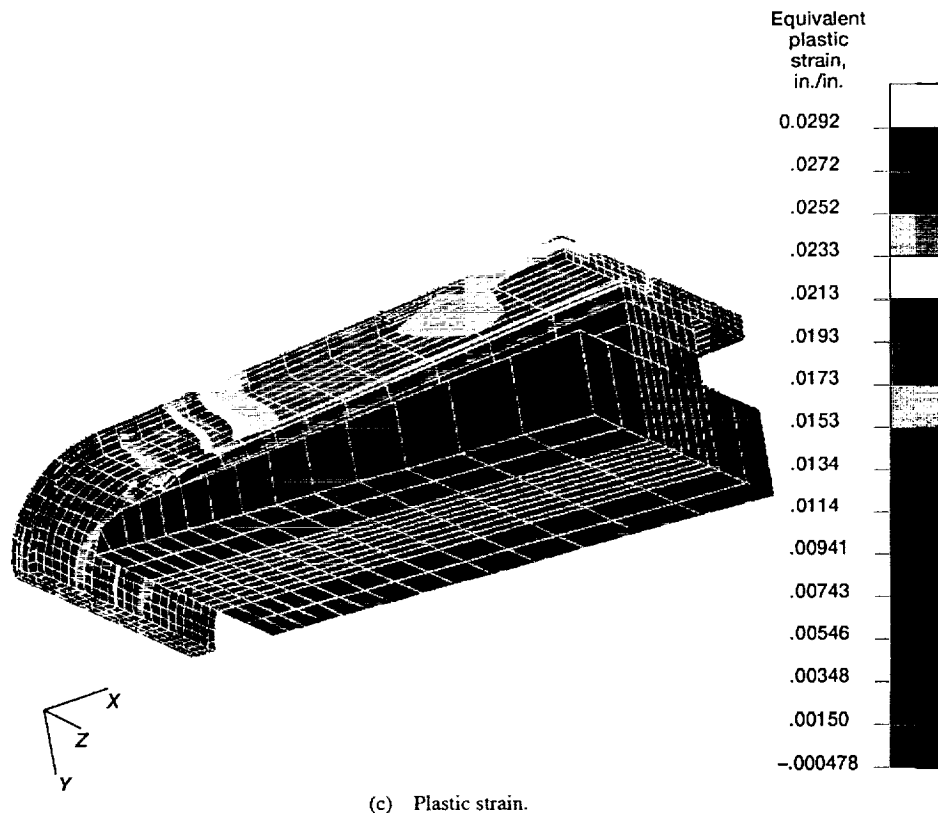


Figure 20.—Concluded.

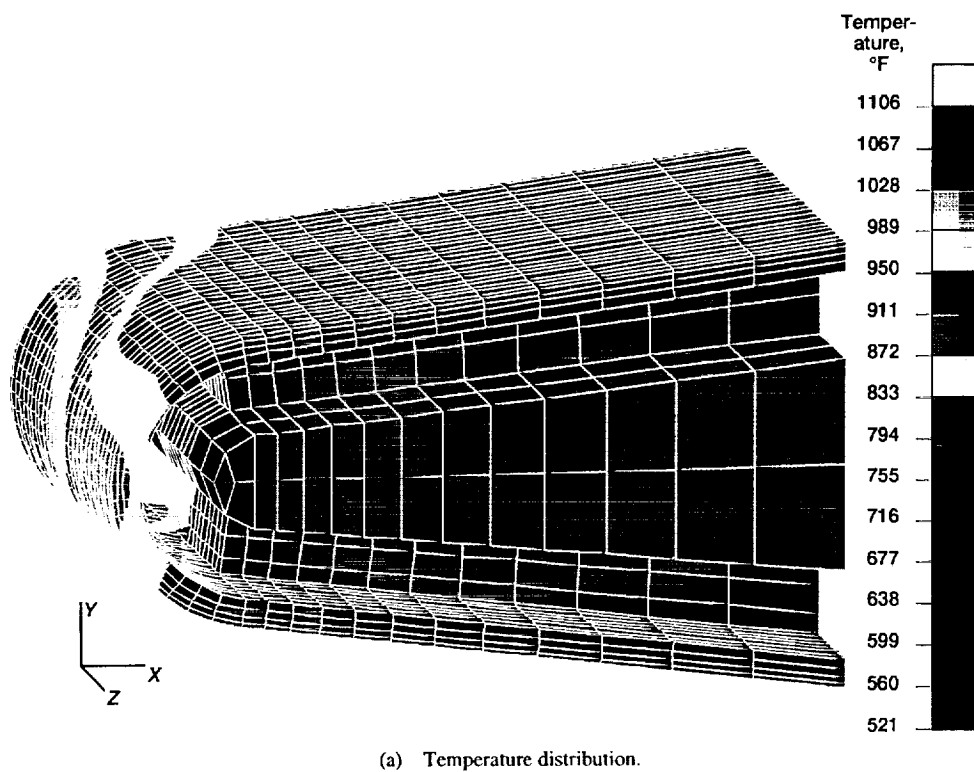
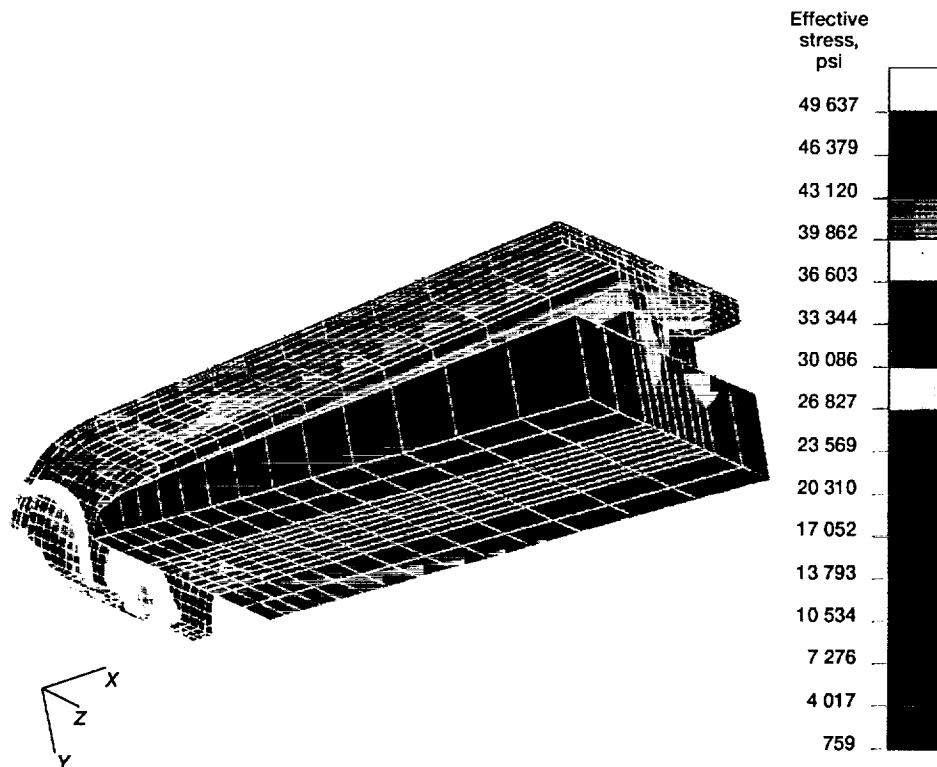


Figure 21.—Model 1 analysis of silicon carbide test specimen and tungsten holder. Combustion temperature, 3000 °F. Coolant supply conditions: flow rate, 0.3 lb/sec; pressure, 60 psia; temperature, 70 °F.



(b) Stress distribution.

Figure 21.—Concluded.

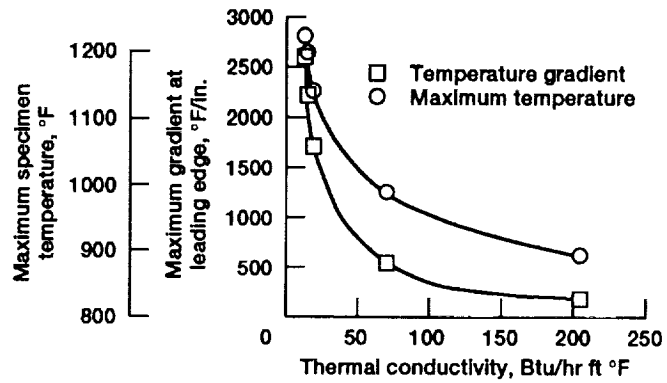


Figure 22.—Maximum specimen temperature and maximum gradient at leading edge as function of thermal conductivity. Combustion temperature, 3000 °F. Coolant supply conditions: flow rate, 0.3 lb/sec; pressure, 60 psia; temperature, 70 °F.

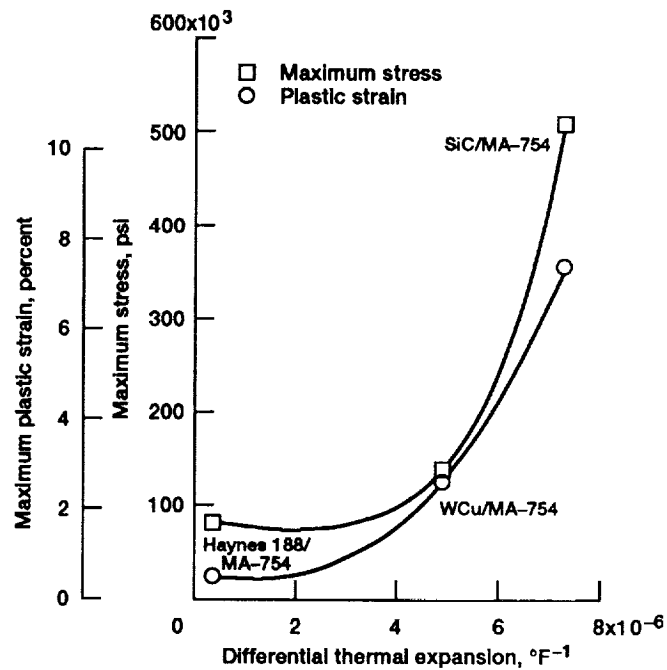
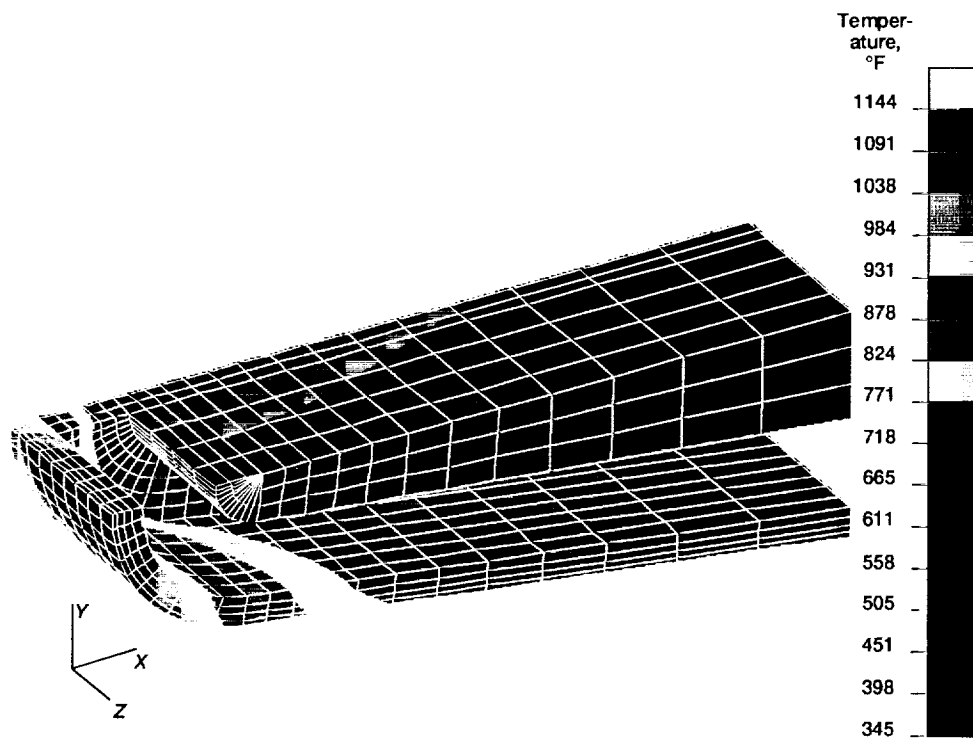
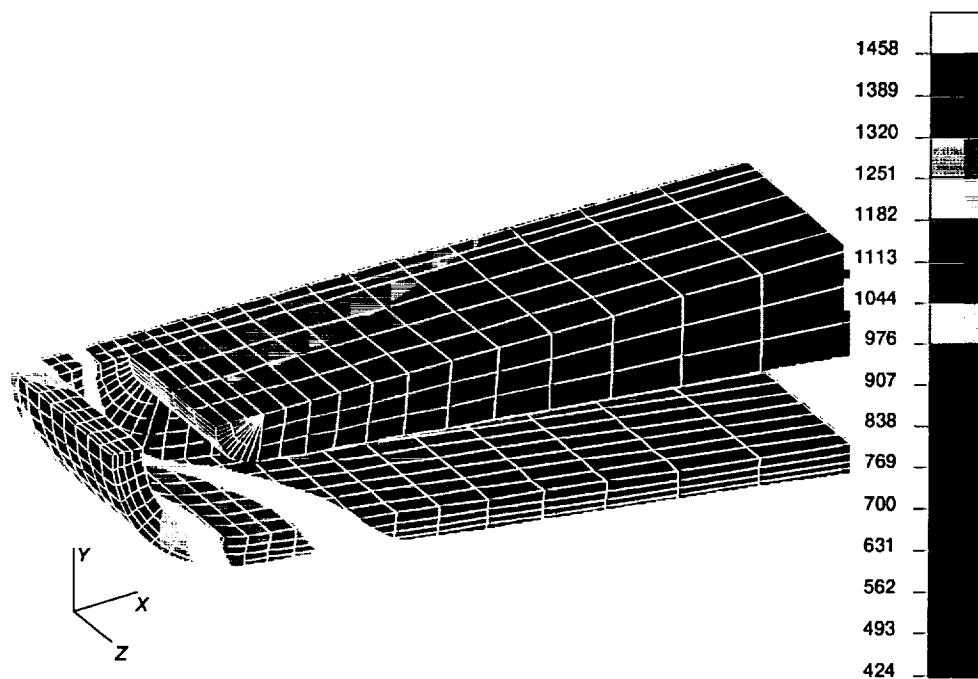


Figure 23.—Maximum stress and maximum plastic strain as function of differences in coefficient of thermal expansion for three material combinations. Combustion temperature, 3000 °F. Coolant supply conditions: flow rate, 0.3 lb/sec; pressure, 60 psia; temperature, 70 °F.



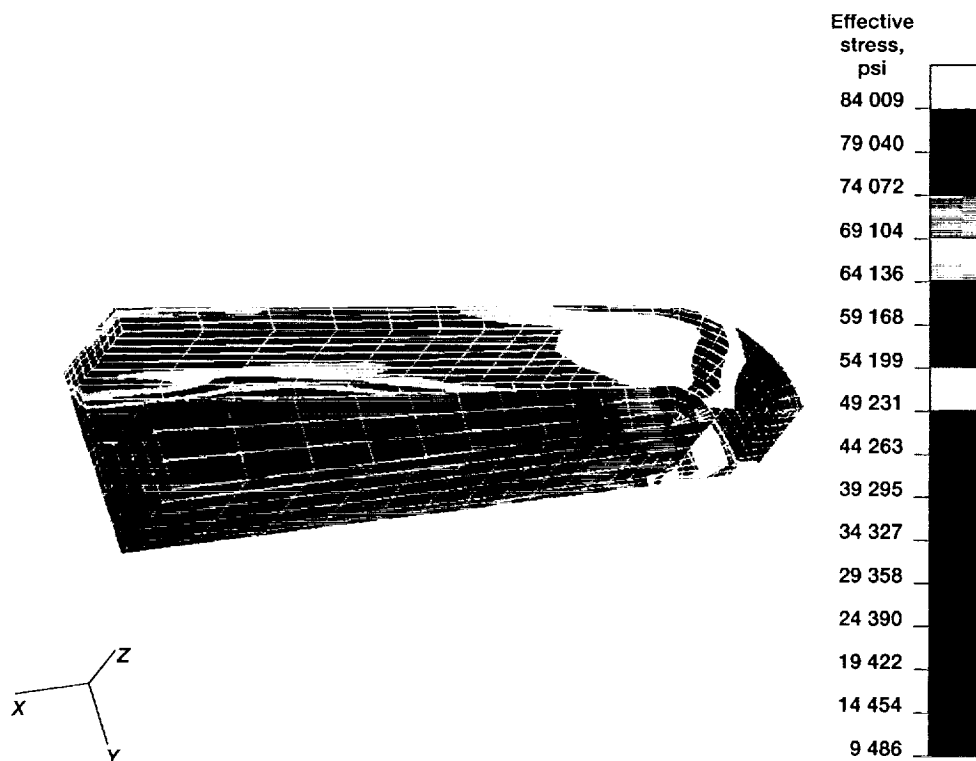
(a) Temperature distribution (3000 °F combustion temperature).



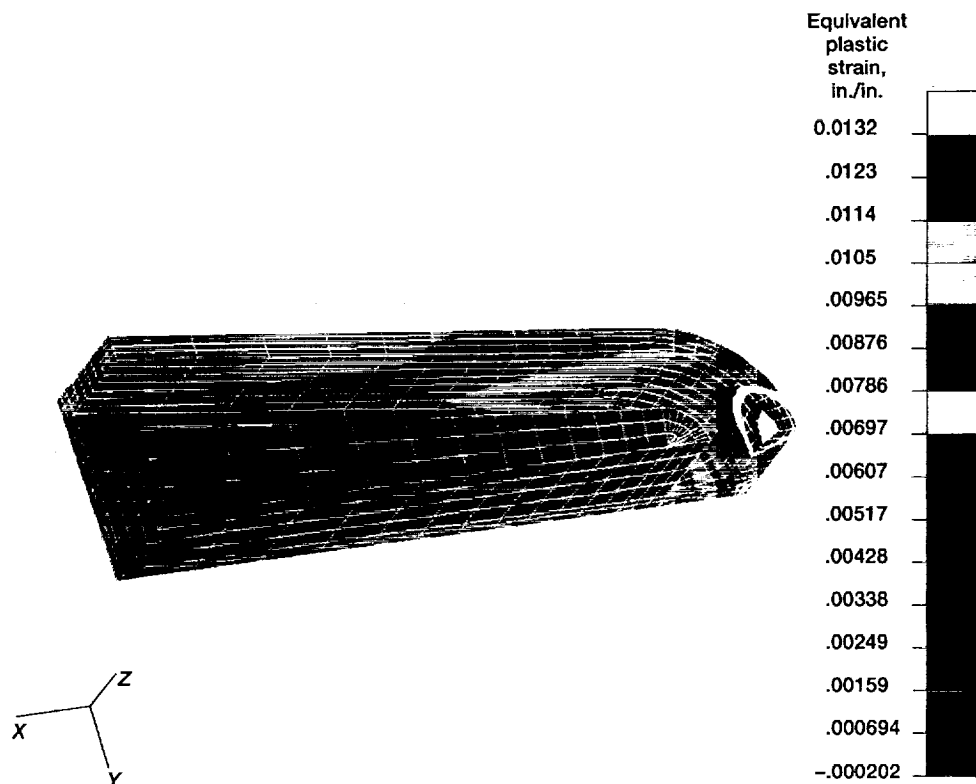
(b) Temperature distribution (4000 °F combustion temperature).

Figure 24.—Model 2 analysis of Inconel MA-754 holder skin and Inconel MA-754 core. Coolant supply conditions: flow rate, 0.3 lb/sec; pressure, 60 psia; temperature, 70 °F.

ORIGINAL PAGE
COLOR PHOTOGRAPH



(c) Stress distribution (4000 °F combustion temperature).



(d) Plastic strain (4000 °F combustion temperature).

Figure 24.—Concluded.

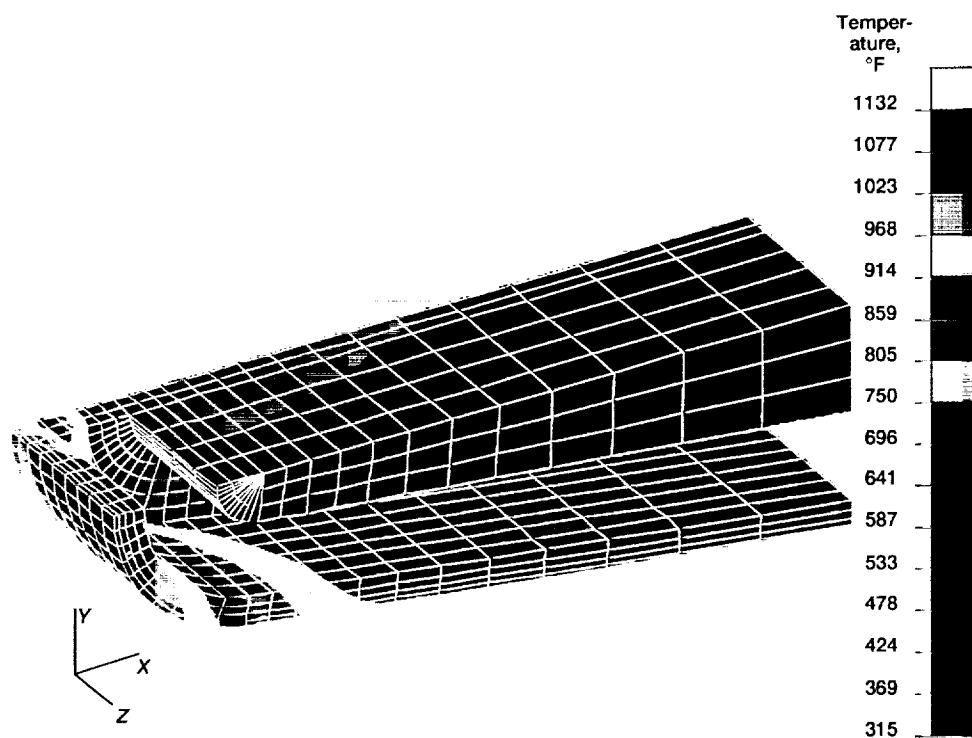


Figure 25.—Model 2 temperature distribution of Haynes 188 holder skin and Inconel MA-754 core. Combustion temperature, 3000 °F. Coolant supply conditions: flow rate, 0.3 lb/sec; pressure, 60 psia; temperature, 70 °F.

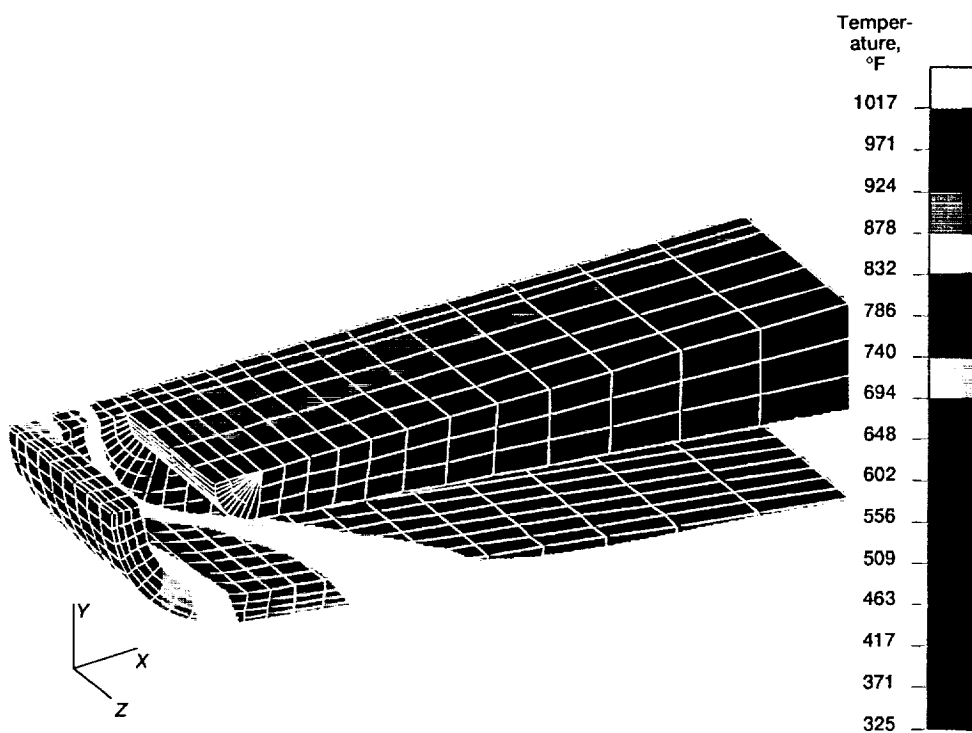
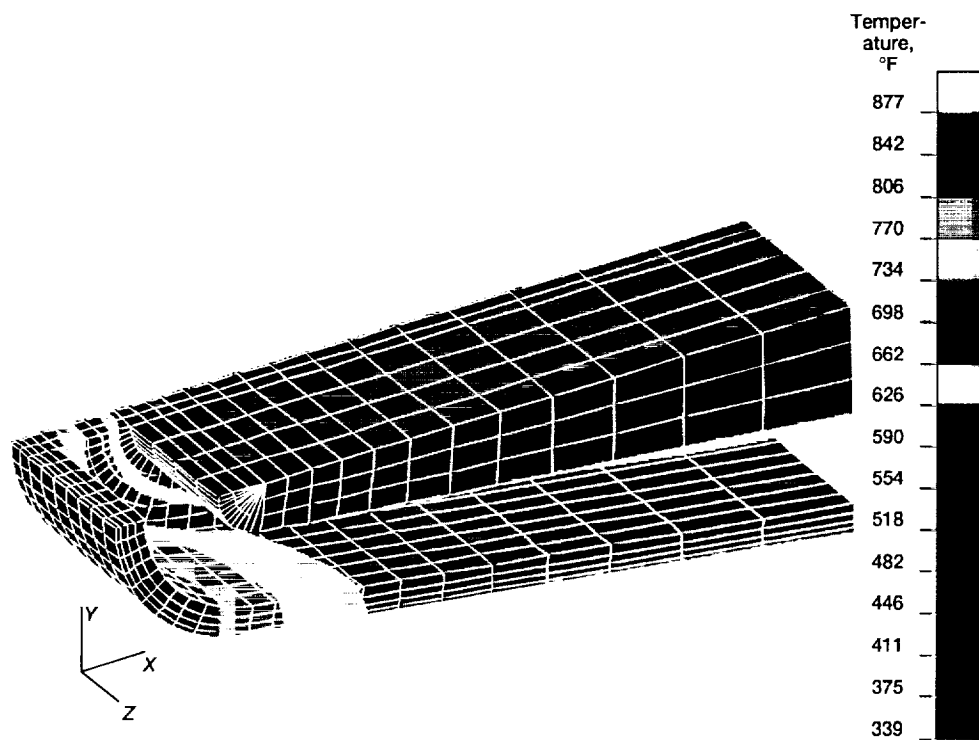
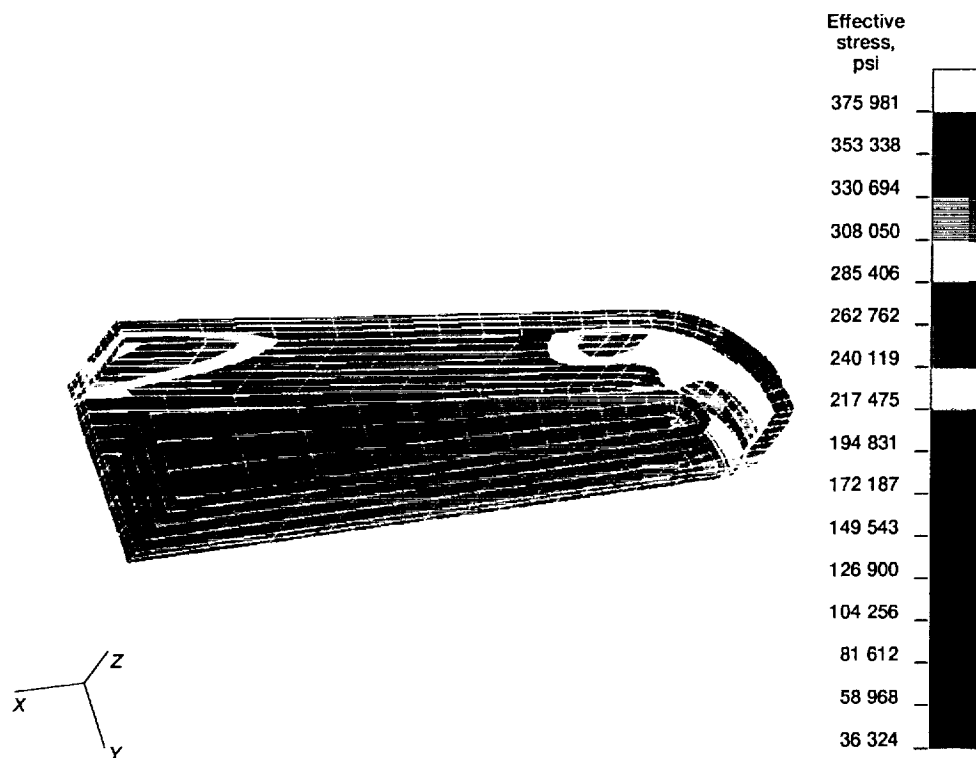


Figure 26.—Model 2 temperature distribution of silicon carbide holder skin and Inconel MA-754 core. Combustion temperature, 3000 °F. Coolant supply conditions: flow rate, 0.3 lb/sec; pressure, 60 psia; temperature, 70 °F.

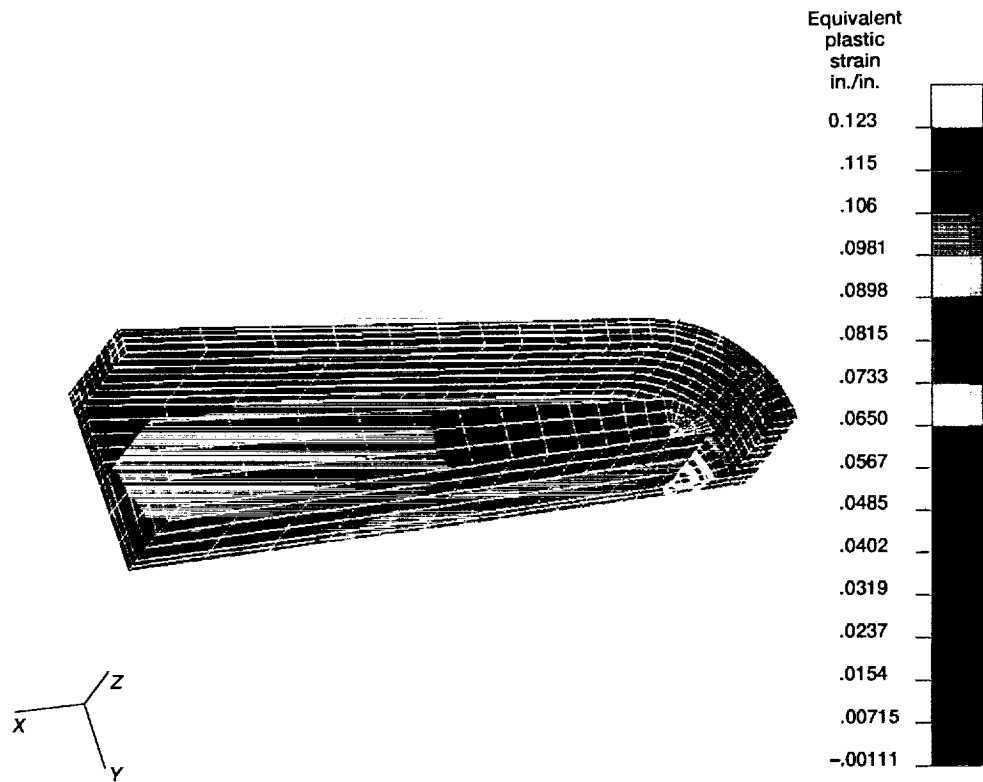


(a) Temperature distribution.



(b) Stress distribution

Figure 27.—Model 2 analysis of tungsten holder skin and Inconel MA-754 core. Combustion temperature, 3000 °F. Coolant supply conditions: flow rate, 0.3 lb/sec; pressure, 60 psia; temperature, 70 °F.



(c) Plastic strain.

Figure 27.—Concluded.

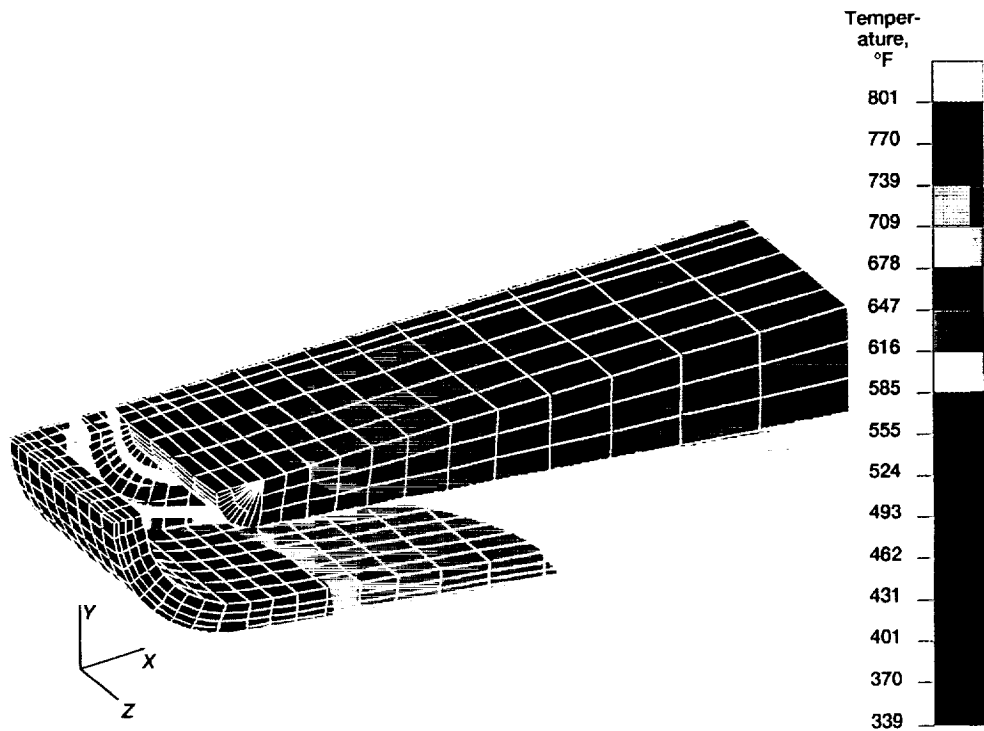
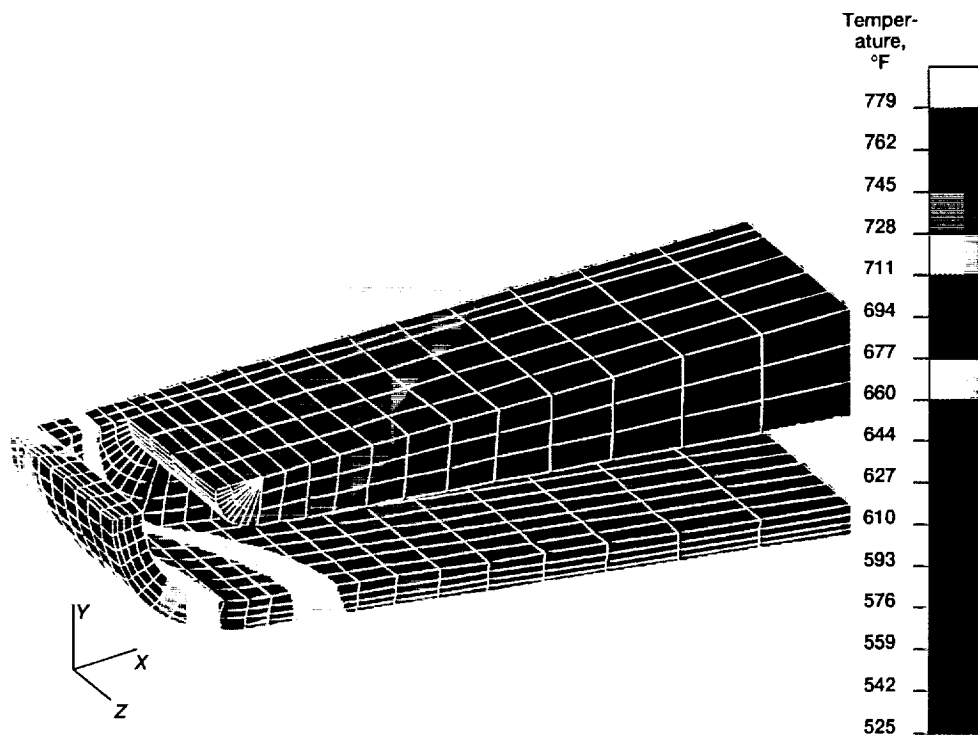
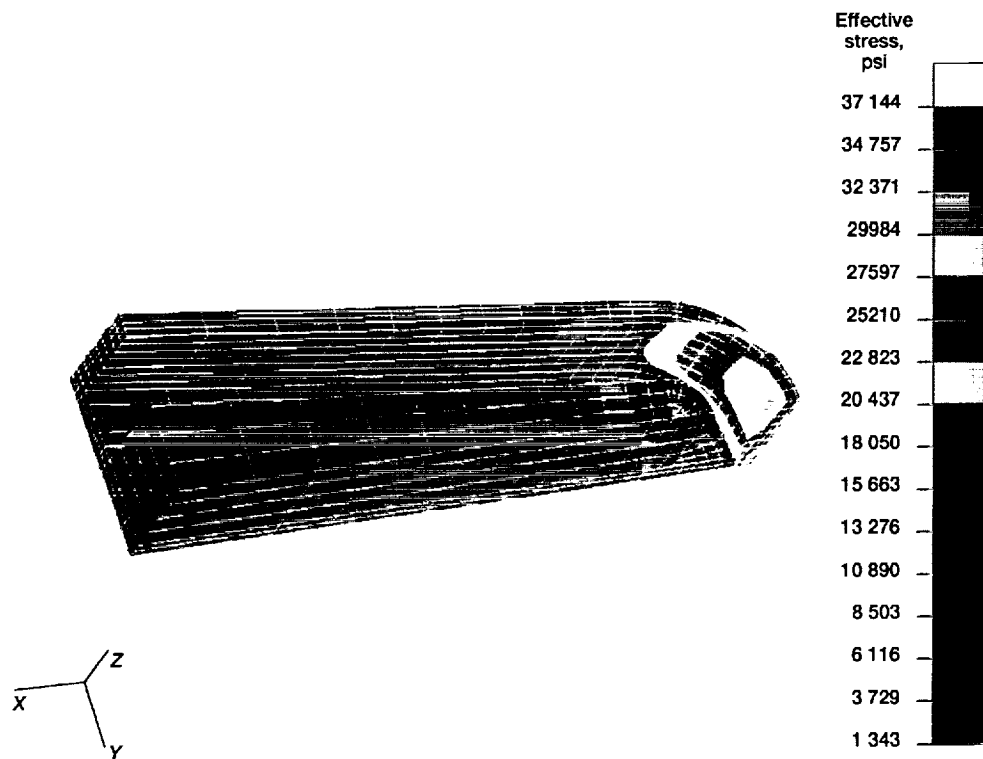


Figure 28.—Model 2 temperature distribution of tungsten/copper holder skin and Inconel MA-754 core. Combustion temperature, 3000 °F. Coolant supply conditions: flow rate, 0.3 lb/sec; pressure, 60 psia; temperature, 70 °F.



(a) Temperature distribution.



(b) Stress distribution.

Figure 29.—Model 2 analysis of tungsten holder skin and tungsten core. Combustion temperature, 3000 °F.
Coolant supply conditions: flow rate, 0.3 lb/sec; pressure, 60 psia; temperature, 70 °F.

ORIGINAL PAGE
COLOR PHOTOGRAPH

REPORT DOCUMENTATION PAGEForm Approved
OMB No. 0704-0188

Public reporting burden for this collection of information is estimated to average 1 hour per response, including the time for reviewing instructions, searching existing data sources, gathering and maintaining the data needed, and completing and reviewing the collection of information. Send comments regarding this burden estimate or any other aspect of this collection of information, including suggestions for reducing this burden, to Washington Headquarters Services, Directorate for Information Operations and Reports, 1215 Jefferson Davis Highway, Suite 1204, Arlington, VA 22202-4302, and to the Office of Management and Budget, Paperwork Reduction Project (0704-0188), Washington, DC 20503.

1. AGENCY USE ONLY (Leave blank)		2. REPORT DATE	3. REPORT TYPE AND DATES COVERED Technical Memorandum	
4. TITLE AND SUBTITLE Design of a High-Temperature Experiment for Evaluating Advanced Structural Materials			5. FUNDING NUMBERS WU - 510 - 01 - 50	
6. AUTHOR(S) Theodore T. Mockler, Mario Castro-Cedeno, Herbert J. Gladden, and Albert Kaufman				
7. PERFORMING ORGANIZATION NAME(S) AND ADDRESS(ES) National Aeronautics and Space Administration Lewis Research Center Cleveland, Ohio 44135 - 3191			8. PERFORMING ORGANIZATION REPORT NUMBER E - 6287	
9. SPONSORING/MONITORING AGENCY NAMES(S) AND ADDRESS(ES) National Aeronautics and Space Administration Washington, D.C. 20546 - 0001			10. SPONSORING/MONITORING AGENCY REPORT NUMBER NASA TM-105833	
11. SUPPLEMENTARY NOTES Theodore T. Mockler, Mario Castro-Cedeno, and Herbert J. Gladden, NASA Lewis Research Center; Albert Kaufman, Analox Corporation, 3001 Aerospace Parkway, Brook Park, Ohio 44142. Responsible person, Theodore T. Mockler, (216) 433 - 8115.				
12a. DISTRIBUTION/AVAILABILITY STATEMENT Unclassified - Unlimited Subject Categories 34 and 39			12b. DISTRIBUTION CODE	
13. ABSTRACT (Maximum 200 words) <p>This report describes the design of an experiment for evaluating monolithic and composite material specimens in a high-temperature environment and subject to high thermal gradients. The material specimens will be exposed to aerothermal loads that correspond to thermally similar engine operating conditions. Materials evaluated in this study were monolithic nickel alloys and silicon carbide. In addition, composites such as tungsten/copper were evaluated. A facility to provide the test environment has been assembled in the Engine Research Building at the Lewis Research Center. The test section of the facility will permit both regular and schlieren photography, thermal imaging, and laser Doppler anemometry. The test environment will be products of hydrogen-air combustion at temperatures from about 1200 °F to as high as 4000 °F. The test chamber pressure will vary up to 60 psia, and the free-stream flow velocity can reach Mach 0.9. The data collected will be used to validate thermal and stress analysis models of the specimen. This process of modeling, testing, and validation is expected to yield enhancements to existing analysis tools and techniques.</p>				
14. SUBJECT TERMS Heat transfer; Thermal/structural analysis; High temperature research; Composite materials; Materials			15. NUMBER OF PAGES 53	
			16. PRICE CODE A04	
17. SECURITY CLASSIFICATION OF REPORT Unclassified	18. SECURITY CLASSIFICATION OF THIS PAGE Unclassified	19. SECURITY CLASSIFICATION OF ABSTRACT Unclassified	20. LIMITATION OF ABSTRACT	